Stall-induced fatigue damage in nonlinear aeroelastic systems under stochastic inflow

Citation for published version:
Tripathi, D, Vishal, S, Bose, C & Venkatramani, J 2022, 'Stall-induced fatigue damage in nonlinear aeroelastic systems under stochastic inflow: Numerical and experimental analyses', *International journal of non-Linear mechanics*, vol. 142, 104003. https://doi.org/10.1016/j.ijnonlinmec.2022.104003

Digital Object Identifier (DOI):
10.1016/j.ijnonlinmec.2022.104003

Link:
Link to publication record in Edinburgh Research Explorer

Document Version:
Peer reviewed version

Published In:
International journal of non-Linear mechanics

Stall-induced fatigue damage in nonlinear aeroelastic systems under stochastic inflow: numerical and experimental analyses

Dheeraj Tripathi[a], Sai Vishal[a], Chandan Bose[b], J Venkatramani[a,*]

[a]*Department of Mechanical Engineering, Shiv Nadar University, India*
[b]*School of Engineering, Institute for Energy Systems, University of Edinburgh, United Kingdom*

Abstract

This study focuses on characterizing the fatigue damage accumulated in nonlinear aeroelastic systems subjected to stochastic inflows through both numerical simulations and wind tunnel experiments. In the mathematical model, nonlinearities are assumed to exist either in the structure (via a cubic hardening nonlinearity in the pitch stiffness), or in the flow (via dynamic stall condition), or simultaneously in both the structural and aerodynamic counterparts. The aerodynamic loads in the attached flow and dynamic stall conditions are estimated using Wagner's formulation and semi-empirical Leishman-Beddoes model, respectively. To augment the findings to in-field flow conditions, the oncoming wind flow is considered to be randomly time-varying in nature. The stochastic input flow fluctuations are modeled using a Karhunen-Loeve Expansion formulation. The response dynamics and the associated fatigue damage of the aeroelastic system, possessing different sources of nonlinearities, are systematically investigated under isolated cases of deterministic and stochastic input flows. Specifically, the pertinent role of stochasticity in the input flow is brought out by presenting the response dynamics and the associated fatigue damage accumulation for different values of noise intensity and time scale of the input flow fluctuation. It is demonstrated that under fluctuating flow conditions, the dynamics intermittently switch between attached flow and the dynamic stall regimes even at low mean flow speeds. The intermittent nature of the response varies as the time scale and intensity of the oncoming flow are varied. The role of torsional stresses as the predominant component dictating the fatigue damage accumulation irrespective of the source of nonlinearity is illustrated. Using the rainflow counting method and Miner's linear damage accumulation theory, it is shown that the accumulated fatigue damage is substantially higher under stochastic flow conditions as compared to deterministic input flows. Importantly, it is observed that different time scales and intensities of the oncoming flow fluctuation play a pivotal role in dictating the fatigue damage in aeroelastic systems. Finally, fatigue damage is observed to be significantly higher for torsionally dominant oscillations in the dynamical stall regime compared to the oscillations at the attached flow regime. The numerical findings are strengthened by drawing comparisons with the preliminary results obtained from wind tunnel experiments performed on a NACA 0012 airfoil undergoing dynamic stall. To the best of our knowledge, this is the first study that systematically bridges the dichotomy between the stall induced dynamical signatures in stochastic aeroelastic systems and maps the same to the corresponding structural damage.

Keywords: *Dynamic stall, Stochastic flow, Fatigue damage, Rainflow counting algorithm, Aeroelastic flutter, Wind tunnel experiments*

1. Introduction

Safe design of aeroelastic systems, such as wind turbine blades and helicopter rotor blades often needs to consider the coupled nonlinear interactions of the elastic and inertial forces of the structure with the unsteady aerodynamic loads. A ubiquitous dynamic phenomenon observed in aeroelastic

*Corresponding author
Email address: j.venkatramani@snu.edu.in (J Venkatramani)

Preprint submitted to International Journal of Non-Linear Mechanics *February 24, 2022*

structures is flutter instability that occurs due to a continuous energy transfer between the structure and the surrounding flow-field. In the presence of nonlinearities in the structure and/or flow, phenomenologically rich bifurcation behavior in the system response is observed [1], which in turn can potentially jeopardize the structural safety of the underlying aeroelastic system [2]. The characteristics of these dynamical responses and the route to flutter have been extensively studied in the literature **by considering a continuous aeroelastic system or a canonical two degrees-of-freedom (DoF) pitch-plunge aeroelastic system [3]. The continuous aeroelastic system can be modelled in different ways such as beam model, shell model etc. [4] and can be solved using finite element based solvers [4, 5, 6]. However, the simplified 2-DoF pitch-plunge aeroelastic model is more commonly used for flutter prediction and is faster and reasonably accurate [3, 7].** Flutter instability in nonlinear aeroelastic systems is marked by the onset of self-sustained Limit Cycle Oscillations (LCOs), typically via a Hopf bifurcation. Under the assumption of the attached flow condition, linear aerodynamic models can predict the dynamical signatures with sufficient accuracy. However, at higher values of instantaneous angles-of-attack, the linear approximations become insufficient with the onset of the dynamic stall phenomenon, involving nonlinear wake effects due to flow separation and vortex shedding [1].

Dynamic stall is commonly encountered in high angle-of-attack applications, such as wind turbine blades, turbomachinery blades, and helicopter blades. An aeroelastic instability occurring at this regime, known as stall flutter, gives rise to large-amplitude pitch-dominated self-sustained oscillations [8]. Aeroelastic analysis of nonlinear structures under dynamic stall conditions has attracted widespread attention in the recent literature [9, 10, 11, 12, 8]. The bifurcation route to stall flutter [9, 10] and the stall flutter characteristics have been thoroughly investigated for different structural configurations, and sources of nonlinearity [11, 12]. Sai Vishal *et al.* [13] showed that a pitch-plunge aeroelastic system subjected to dynamic stall conditions could exhibit stall or classical flutter response - depending on the particular route to synchronization. It is worth noting the fact that most of these studies are carried out assuming uniform flow conditions. However, in actual field conditions, aerodynamic loads on structures like wind turbines and helicopter rotor blades are often highly stochastic in nature due to the variation of flow speed with time and/or height in the atmospheric boundary layer. Recent studies by Bethi *et al.* [14], and Devathi and Sarkar [15] highlight the significance of adopting a stochastic flow model and studying the subsequent impact on the aeroelastic response dynamics. The authors have shown the presence of noise-induced intermittency (NII) even at low mean flow speeds, triggered due to the input flow fluctuations. In a recent study, dos Santos and Marques [16] showed that, depending on the intensity of flow fluctuations, the aeroelastic structures enter high amplitude stall flutter regimes, and the probability of reaching divergent oscillations increases rapidly, even at speeds below the linear flutter boundary.

Aeroelastic structures exhibiting stall flutter oscillations at high angles-of-attack have been speculated to be more susceptible to fatigue-induced failure as compared to classical flutter [17, 18]. A distinct trait of stall flutter is the torsional dominance in the high-amplitude LCOs [7]. Most materials used in the engineering applications are prone to failures due to torsional stresses [19], necessitating an in-depth investigation of the structures exhibiting stall flutter from the standpoint of structural health monitoring. Additionally, the impact of stall-induced oscillations (as well as classical flutter oscillations) in the presence of stochastic inflow on structural damage has received less attention in the aeroelastic literature. This can be attributed to the fact that failure determination due to the aging effects such as fatigue accumulation is a challenging problem to date due to the uncertainties associated with the time-varying loads. Although the studies on fatigue damage for constant and variable amplitude loading and associated crack growth mechanisms have been performed for various aeroelastic applications like suspension bridges [20], wind turbines [19], aircrafts [21], similar studies addressing the effects of structural and aerodynamic nonlinearities are limited [22, 19] in hitherto literature. Sarkar *et al.*[22] investigated the fatigue damage induced in a randomly vibrating 1-DoF aeroelastic system in the presence of fluctuating flow under dynamic stall conditions using the ONERA model. Although the authors demonstrated the impact of flow uncertainty on fatigue damage, the aeroelastic structure was modeled using a rather simplistic 1-DoF model. Further, the impact of the discontinuous nonlinearity arising from dynamic stall conditions was not investigated due to the ONERA aerodynamic model's limitations. Venkatesh *et al.*[19] investigated the effect of uncertainties on the fatigue damage of wind turbine blades and noted that random flow fluctuations pose a greater threat to the structural integrity as compared to parametric uncertainty. However, the flow was considered attached, and hence, does not incorporate the effects of aerodynamic nonlinearity associated with the flow separation. In light of these studies, the present paper aims to investigate the effect of stochastic inflow on nonlinear pitch-plunge aeroelastic systems from the standpoint of structural safety.

It is worth noting that the hitherto studies, be it for dynamics or fatigue damage analysis, have considered either a low-order 1-DoF structural model and a semi-empirical dynamic stall aerodynamic model [22] or a 2-DoF structural model with linear aerodynamic model [19]. However, a 2-DoF airfoil model gives rise to rich dynamical signatures that the 1-DoF model does not capture. Galvanetto *et al.*[10] reports aperiodic oscillations in the bifurcation characteristics of a 2-DoF aeroelastic system under the stall. Similar observations entailing a period-doubling route to chaos were noted by Sarkar and Bijl[9] in a 2-DoF aeroelastic system subjected to dynamic stall. On the other hand, only a transition to LCOs via a Hopf bifurcation is reported in typical 1-DoF stall flutter problem [23]. Furthermore, the hitherto literature on aeroelastic fatigue damage studies does not consider the combined effect of coupled structural and aerodynamic nonlinearities that can give rise to radically different response dynamics compared to isolated nonlinearities, either in the structure or in the aerodynamics [24]. Furthermore, the presence of random input flow fluctuations may significantly alter the bifurcation scenario and result in the loss of stability under critical conditions [25, 26, 27]. Therefore, the incurred fatigue damage in these scenarios will be qualitatively and quantitatively distinct from that reported in the existing literature. To that end, structural health monitoring of in-field aeroelastic systems demands a systematic investigation under the combined effect of structural and aerodynamic nonlinearities with the additional complexity of random input flows. A comparative study of the fatigue damage induced in the cases of coupled nonlinearities with that of the isolated cases is essential. Similarly, comparing damage values obtained in scenarios involving deterministic flows against stochastic input flow fluctuations can provide crucial insights into the structural safety of nonlinear aeroelastic systems under gusty conditions. Furthermore, the role of probabilistic markers such as noise intensity and time scales of the input flow behind the fatigue damage accumulation is not clear in terms of triggering NII [25]. **Indeed, typical flexible structures such as unmanned aerial vehicles (UAVs) [28], wind turbine blades [29], and helicopter blades [30] are often subjected to dynamic stall, hand-in-hand with stochastically fluctuating wind loads. While the ability of aeroelastic systems to display large amplitude periodic oscillations (often LCOs) has motivated the community to estimate fatigue damage incurred using RFC [22, 19], the ability of noise-induced dynamical signatures like intermittency to incur fatigue damage in aeroelastic systems remains unanswered. In wake of low-flow applications like wind turbine blade etc to be subjected to both noisy wind flow and dynamic stall behavior, attempting to present the safety of noise-induced responses in stochastic stall flutter problems is an immediate need.** To the best of the authors' knowledge, there have been minimal efforts to systematically document the role of coupled structural and aerodynamic nonlinearities and input flow fluctuations (and its probabilistic markers) hand-in-hand behind the incurred fatigue damage. The present study is devoted to taking up this analysis.

In this study, a 2-DoF pitch-plunge aeroelastic system subjected to randomly fluctuating loads is considered that exhibits flutter oscillations, arising either under attached flow (linear aerodynamics) or dynamic stall conditions (nonlinear aerodynamics). The accumulated fatigue damage in the structure is compared in these two scenarios. The structure is assumed to possess a cubic hardening nonlinearity in the pitch DoF unless stated otherwise. The nonlinear aerodynamic loads at high angles-of-attacks during stall flutter are calculated using the Leishman-Beddoes (LB) semi-empirical dynamic stall model [31], and the loads in the attached flow regimes (which in turn give rise to classical flutter) are calculated using Wagner's function-based unsteady formulation. The random fluctuations in the flow are incorporated using the Karhunen-Loeve Expansion (KLE) formulation [25]. The response dynamics of the system at attached flow and dynamic stall regimes for flow speeds lying below and above the linear flutter boundary are systematically laid out for both deterministic and stochastic inflow scenarios. As a first step to investigate the fatigue damage from the earlier investigated aeroelastic responses, the locations of maximum stress applied on the airfoil geometry, referred to as critical points, are identified. Then, the corresponding stress cycles are calculated using the rainflow counting (RFC) algorithm [32]. The RFC algorithm can model random stress cycles that arise, essentially due to the NII signatures of the response dynamics, and is widely used for estimating fatigue damage in most engineering applications. Finally, the linear damage accumulation rule developed by Miner [33], based on Palmgren's linear accumulation theory [34], is combined with the RFC algorithm to obtain the cumulative fatigue damage induced in the airfoil for both classical and stall flutter cases. Finally, the findings are compared against nonlinear aeroelastic scenarios involving deterministic flows. In a nutshell, the focal points of the present study are as follows: (i) to investigate the effect of coupled structural and aerodynamic nonlinearity on response dynamics of the aeroelastic structure under fluctuating inflow, (ii) to analyze the effect of the time scales of oncoming flow on aeroelastic responses, and iii) to compare the resultant fatigue damage in structure due to different sources of nonlinearity under different time scales of fluctuating inflow.

The rest of this paper is organized in the following sections. Section 2 depicts the mathematical formulation of structural equations, aerodynamic loads, the stochastic model used to incorporate the random fluctuations in the flow, and the methodology deployed to compute the fatigue damage. Section 3 presents a comparison of the aeroelastic responses at attached flow and dynamic stall regimes for deterministic and stochastic cases. Section 4 details the methods used to calculate the critical points and stress cycles. Then, the estimated fatigue loads for the corresponding cases, investigated in Section 3, are presented. A preliminary experimental investigation into stall induced oscillations and corresponding fatigue damage analysis is presented in Section 5. Finally, the salient findings of the study are summarized in Section 6. **To summarize the objectives of this work, a schematic illustrating the outline of the problem with the methodology and the end-outcome of fatigue damage is presented in Fig. 1.**

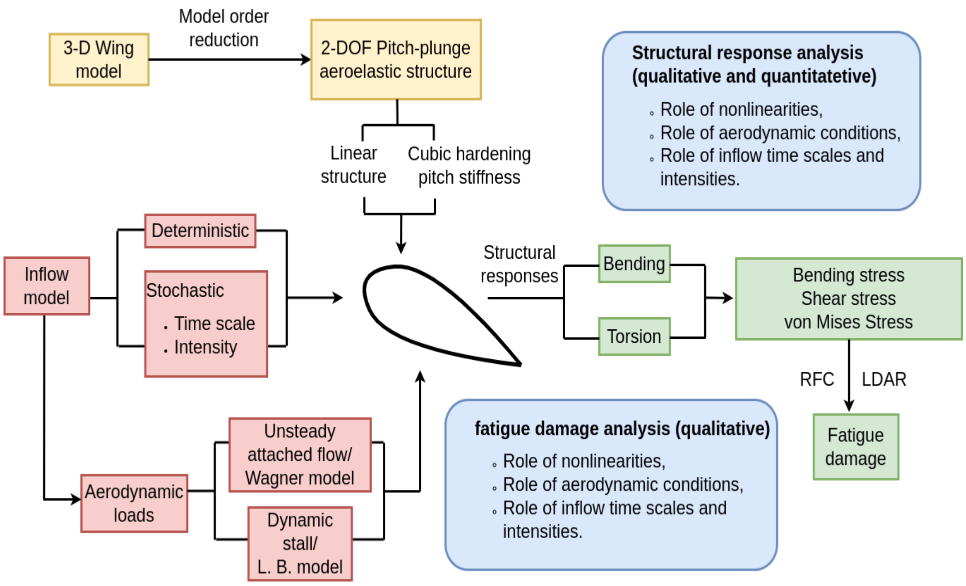

Figure 1: Schematic representation of the work-flow involved in this study.

2. Mathematical model of the aeroelastic system

2.1. Structural model

A 2-DoF aeroelastic system, exhibiting pitch (α) and plunge (ξ) motion through the torsional and translational springs, respectively, is considered for the present study. The schematic of the representative airfoil-spring system is shown in Fig. 2. Here, $b = c/2$ denotes the semi-chord length, where c is the chord-length. a_h is the nondimensional length of mid-chord from the elastic axis, and x_α is the nondimensional length of the mass center from the elastic axis; both the lengths are considered to be positive towards the trailing edge and are nondimensionalized with the value of b. k_ξ and k_α represent bending and torsional stiffness, respectively. The structural damping is assumed

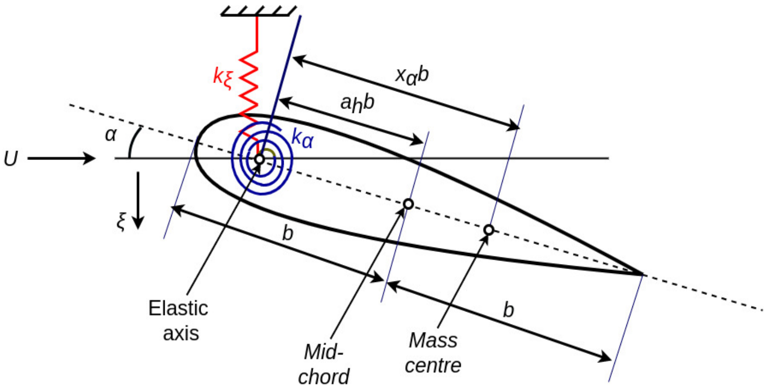

Figure 2: Schematic representation of the pitch-plunge aeroelastic system. The airfoil section is considered to be NACA 0012.

to be zero in the present study [3]. For a 2-DoF pitch-plunge aerofoil, the equations of motion in the nondimensional form are given by [3]

$$\xi'' + x_\alpha \alpha'' + \left(\frac{\bar{\omega}}{U}\right)^2 \xi = -\frac{1}{\pi\mu} C_l(\tau), \tag{1}$$

$$\frac{x_\alpha}{{r_\alpha}^2}\xi'' + \alpha'' + \left(\frac{1}{U}\right)^2 (\alpha + \beta_\alpha \alpha^3) = \frac{2}{\pi\mu {r_\alpha}^2} C_m(\tau). \tag{2}$$

Here, $\xi = h/b$ is the nondimensional plunge displacement, where h denotes the dimensional plunge deflection and is positive in downward direction. α is the nondimensional pitch angle about the elastic axis, considered to be positive at nose up. $\bar{\omega}$ is the ratio of the dimensional natural frequencies of plunge (ω_ξ) and pitch (ω_α). $U = V/b\omega_\alpha$ is the nondimensional flow speed, where V is the dimensional free-stream velocity. $\mu = m_a/\pi\rho b^2$ represents the nondimensional mass ratio, where m_a is the airfoil mass and ρ is the density of the air. The pitch and plunge stiffness in their nondimensional form are represented as a function of their respective displacements.

To compare the fatigue damage accumulation between a linear and a nonlinear aeroelastic system, a linear and a cubic hardening stiffness in the pitch DoF are considered, respectively. A generic function representing the pitch stiffness is provided in Eq. 2, where β_α is the nondimensional coefficient of cubic stiffness in pitch. It should be noted that β_α value becomes zero when the system is linear. The plunge stiffness is considered to be linear throughout the study. $\tau = Vt/b$ is the nondimensional time, where t is the dimensional time and r_α represents the nondimensional radius of gyration about the elastic axis given by $r_\alpha = \sqrt{I_\alpha/m_a b^2}$, where I_α is the moment of inertia about pitch. C_l and C_m denote the aerodynamic lift and moment coefficients, respectively. The mathematical formulation to estimate the aerodynamic load coefficients is presented in the following subsection.

2.2. Aerodynamic model

The present study investigates the response dynamics and the corresponding fatigue damage of the system under attached flow and dynamic stall conditions. The aerodynamic load coefficients under attached flow conditions, considering the flow to be inviscid and incompressible, the lift and moment coefficients are estimated using Wagner's unsteady aerodynamic formulation in the time domain [3]. The expression to obtain the load coefficients is given by,

$$\begin{aligned} C_l(\tau) = \pi(\xi'' - a_h\alpha'' + \alpha') + 2\pi[\alpha(0) + \xi'(0) + (0.5 - a_h)\alpha'(0)]\phi(\tau) + \\ 2\pi\int_0^\tau \phi(\tau - \tau_0)[\alpha'(\tau_0) + \xi''(\tau_0) + (0.5 - a_h)\alpha''(\tau_0)]d\tau_0, \end{aligned} \tag{3}$$

$$C_m(\tau) = \pi(0.5 + a_h)[\alpha(0) + \xi'(0) + (0.5 - a_h)\alpha'(0)]\phi(\tau) + \pi(0.5 + a_h) \times \int_0^\tau \phi(\tau - \tau_0)[\alpha'(\tau_0) + \xi''(\tau_0) + (0.5 - a_h)\alpha''(\tau_0)]d\tau_0 + \frac{\pi}{2}a_h(\xi'' - a_h\alpha'') - (0.5 - a_h)\frac{\pi}{2}\alpha' - \frac{\pi}{16}\alpha''. \quad (4)$$

Here, $\phi(\tau)$ is the Wagner function given by $\phi(\tau) = 1 - 0.165\mathrm{e}^{(-0.0455\tau)} - 0.335\mathrm{e}^{(-0.3\tau)}$. The expression were simplified further and integrated into the equations of motion (see Eqs. 1 and 2) in order to obtain a state-space formulation of first order ordinary differential equations (ODEs). The present study adopts the state-space formulation to calculate the loads at attached flow regime and the details of the same are found out in Lee *et al.*[3]. The initial conditions for pitch, pitch rate, plunge and plunge velocity are chosen as $\alpha(0) = \pi/12$, $\alpha'(0) = 0$, $\xi(0) = 0$ and $\xi'(0) = 0$ in the present study. **Note that this initial condition provides an initial incident angle higher than the static stall angle [35].**

Modeling of aerodynamic loads under dynamic stall conditions involves accounting for different stages, such as flow separation, vortex shedding, and flow reattachment phases [1], including the loads at the attached flow regime. The variation of load coefficients becomes highly nonlinear in the flow separation and vortex shedding regimes, which need to be accurately modeled either using high fidelity Navier–Stokes solvers [28] or semi-empirical models [35]. Although Navier–Stokes solvers provide an accurate estimation of the aerodynamic loads, they are computationally expensive. Alternatively, semi-empirical models, such as LB model [35] are capable of estimating the loads with an agreeable extent of accuracy while considerably reducing the computation cost. They are widely used in the literature for aeroelastic computations of systems subjected to dynamic stall [10, 12, 14, 15]. Accordingly, the present study uses the LB model to estimate the loads at dynamic stall regimes.

The LB model was initially developed in the indicial form [30] using the experimental data of aerodynamic loads at subsonic speed regimes (Mach number $(M) < 0.8$) and has subsequently been modified into state-space forms [31, 29] for various engineering applications. The LB model uses parameters obtained from static and dynamic stall tests to demarcate the flow regimes and estimate the load coefficients at regular intervals of M values in the subsonic regime. The state-space formulation serves to be advantageous for stability and response analysis as it can be directly coupled with the structural governing equations, and the ODEs in the abridged form are given by [10],

$$x' = f(x, \hat{\alpha}, q), \quad (5)$$

where $x = [x_1, x_2, ..., x_{12}]^T$ are twelve aerodynamic states used to calculate the aerodynamic loads representing the unsteady attached flow, flow separation, vortex shedding, and flow reattachment regimes. q represents the nondimensional effective pitch rate, given by $q = 2\alpha'$ and $\hat{\alpha}$ denotes the effective angle of incidence, given by

$$\hat{\alpha} = \tan^{-1}\left(\frac{\sin\alpha + \xi'\cos\alpha}{\cos\alpha - \xi'\sin\alpha}\right). \quad (6)$$

The aerodynamic forces in the LB model are expressed as components perpendicular and parallel to the airfoil chord as it serves to be more convenient in calculations involving rotor blade applications [10]. The coefficients of forces are given as

$$\begin{Bmatrix} C_n \\ C_m \\ C_c \end{Bmatrix} = g(x, \alpha, q), \quad (7)$$

where C_c and C_n represent the coefficients of aerodynamic loads with respect to the chord and the normal, respectively. However, the equations of motion require the estimation of lift force (see Eqs.

(1) and (2)) which acts perpendicular to the wind flow. In such case, the coefficient of lift (C_l) can be resolved such that,

$$C_l = C_n \cos\alpha - C_c \sin\alpha. \tag{8}$$

The moment and normal force coefficients are estimated using the superposition of loads coefficient components at each flow module. The LB model is divided into three modules: (i) Unsteady attached flow module - The load coefficients are calculated using the first eight states ($x_1 - x_8$) which are modified from Wagner's unsteady formulation by accounting for the compressibility factor of flow, (ii) Trailing edge separation and reattachment module - the change in load coefficients with respect to the amount of flow separation calculated using the states x_9, x_{10} and x_{12}, and (iii) Dynamic stall or vortex-induced aerodynamic loads - additional loads arising due to the formation of the vortex on the airfoil surface calculated by state x_{11}. The total loads are given as the summation of aerodynamic forces from each module by,

$$C_n = C_n^I + C_n^f + C_n^v, \quad C_m = C_m^I + C_m^f + C_m^v, \quad C_c = C_c^f. \tag{9}$$

The superscripts, I, f, and v indicate impulsive loads from the attached flow component, trailing edge separation component, and vortex shedding component, respectively. A detailed description of the formulation of aerodynamic loads and values of Mach number dependent parameters at regular intervals of M in the range of 0.3 - 0.8 (the M concerned with the present study ranges from 0.3 - 0.6) can be found in [30, 10, 14] and is not presented here for the sake of brevity. Since the present study involves accounting for random fluctuations in the flow, giving rise to fluctuations in M as well, the Mach number dependent empirical parameters inherently become time-varying and need to be estimated at each time step. Since the empirical parameter values are only known corresponding to specific M values, at intermediate values of M, a cubic Hermite interpolating polynomial function is used to estimate the Mach number dependent parameters. The cubic Hermite interpolation polynomial ensures C^1 continuity which means the fitted curve is continuously differentiable at the known data points. Finally, aeroelastic equations of motion (Eqs. (1) and (2)) are converted to four first-order ODEs such that,

$$\begin{Bmatrix} x'_{13} \\ x'_{14} \\ x'_{15} \\ x'_{16} \end{Bmatrix} = \hat{f}(\alpha, \alpha', \xi, \xi', C_l, C_m). \tag{10}$$

Here, the state variables x_{13}, x_{14}, x_{15} and x_{16} represent α, α', ξ and ξ', respectively - which are solved using numerical integration.

2.3. Karhunen-Loeve Expansion for fluctuating inflow

The fluctuations in the longitudinal inflow are generated using the Karhunen-Loeve expansion (KLE) approach using a prescribed correlation [15, 25]. In KLE, a stochastic process is simulated as bi-orthogonal decomposition of its correlation function [26]. This essentially means that the on-coming flow is represented as a random process involving a series expansion of a set of deterministic functions $u_i(\tau)$ and a vector of independent orthogonal random variables $\eta_i(\theta)$, defined in the probability space ($\mathit{\Omega}$, ξ, P) and $\theta \in \omega$ (where ω is the sample space). The stochastic inflow velocity is given by

$$U(\tau, \theta) = U_m + \sum_{i \geq 1} \sqrt{\lambda_i} u_i(\tau) \eta_i(\theta). \tag{11}$$

For the ease of representation, dependence on θ is dropped in this paper. The deterministic functions $u_i(\tau)$ are obtained by solving Fredholm's equation of the second kind [36] given by

$$\int_{\Omega} C(\tau, \tau').u_i(\tau')\, d\tau = \lambda_i u_i(\tau), \tag{12}$$

where $C(\tau, \tau')$ is the correlation function of $U(\tau)$. Note that $U(\tau)$ is assumed to be a Gaussian process with a target auto-correlation function

$$R_{UU,tgt}(\tau) = \sigma^2.e^{-c_1 {\tau_{lag}}^2}. \tag{13}$$

Here, σ^2 is the variance of the process, τ_{lag} is the time lag and c_1 is the correlation coefficient that governs the fluctuation time scale. The number of terms needed for simulating Eq. 11 is the minimum "z" satisfying

$$\sum_{i=1}^{z} \lambda_i \geq 0.99 \sum_{i=1}^{n} \lambda_i, \tag{14}$$

where n is the total number of eigenvalues obtained from the discrete form of Eq. 12.

2.4. Time scale of the oncoming flow

In field conditions, the oncoming flow comprises different time scales depending upon natural conditions. While studies in the dynamical systems literature are rife with examples, illustrating the role played by the time scales of the input noise over the bifurcation characteristics [37], we specifically focus on the aeroelastic findings presented by Venkatramani *et al.*[25]. For a classical flutter system, it was shown that based on the correlation length of the input flow and the system time scale (here, the LCO time period), stochastic input flows could be classified into 'long' and 'short' time scale flow fluctuations. These long or short time scales can individually produce radically distinct dynamics (at distinct stability regimes). Therefore, an interplay between different time scales (c_1) and noise intensity (σ) on the aeroelastic dynamics, and in turn the incurred fatigue damage is investigated in this study. Accordingly, three different types of fluctuating inflows with varying time-scales are considered in the present study: i) '*Type A*' (c_1 = 0.01, correlation length ($\tau_{l,A}$) = 30), ii) '*Type B*' (c_1 = 0.001, correlation length ($\tau_{l,B}$) = 100) and, iii) '*Type C*' (c_1 = 0.00001, correlation length ($\tau_{l,C}$) = 1000). Here, the correlation length is defined as τ_{lag} needed for $R_{UU,tgt}(\tau)$ to approach zero [25].

The chosen fluctuating inflows are classified as long time scale or short time scale by comparing their correlation length with nondimensional system time scale (τ_{sys}) [25], which is found to be 70 in the present system. Hence, '*Type A*' inflow is representative of a short time scale (since $\tau_{l,A} < \tau_{sys}$); whereas, '*Type B*' and '*Type C*' inflows are indicative of long time scales (since $\tau_{l,B}$ and $\tau_{l,C} > \tau_{sys}$). Figures 3(a)-(c) show the variation of flow speed with time simulated for $U_m = 6$ and $\sigma = 0.3$ and representing fluctuating inflow model '*Type A*', '*Type B*' and '*Type C*', respectively. The corresponding correlation functions are presented in Figs. 3(d)-(f), respectively. It is observed that the amplitude of $U(\tau)$ also increases as the correlation length of fluctuating inflow increases. In the light of the objective of this study to investigate the role of time scales and noise intensity of the input flow fluctuations on the response dynamics and the corresponding structural safety, we choose three different noise intensities in the present study. Accordingly, the values of σ are chosen as 0.1, 0.2 and 0.3. It is worthwhile to mention that a variation in σ is assumed not to affect the correlation length of fluctuating inflow significantly and therefore elucidating the need for investigating the effects of time scales and noise intensity of $U(\tau)$ as isolated cases.

2.5. Validation of dynamic stall model under stochastic inflow condition

The solver's efficacy in estimating the aerodynamic loads in the dynamic stall regime under fluctuating flow conditions is inspected in the present subsection. This is done by first comparing the value of C_m calculated using the LB model to the findings from dynamic stall experiments by McAlister *et al.*[38] under deterministic flow conditions. The comparison of the C_m vs α hysteresis plot for an airfoil, undergoing forced sinusoidal pitching prescribed as: $\alpha(\tau) = 12 + 10\sin(\kappa\tau)$, with the reduced frequency $\kappa = \omega b/V = 0.0976$, obtained from present computation and experiments at $M = 0.3$ is shown in Fig. 4(a). The hysteresis plot is observed to be in close agreement with the experimental result substantiating the model's validity in the dynamic stall regime.

Next, the present LB model is examined for the fluctuating flow conditions with the same pitching kinematics. The resulting fluctuations in the M at each time step are incorporated in the model

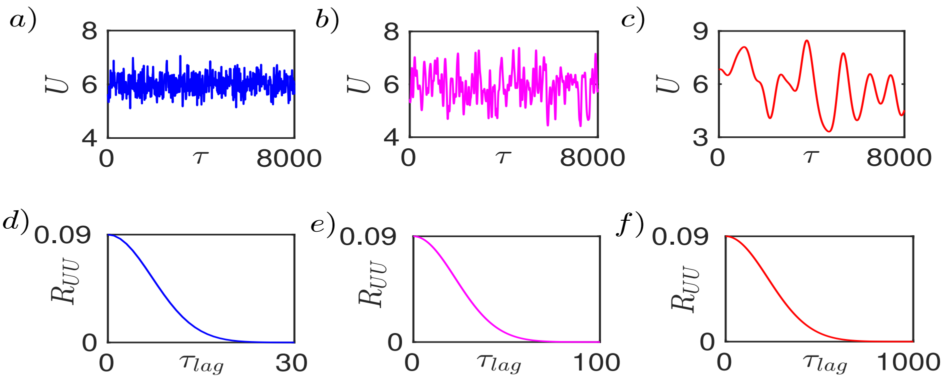

Figure 3: Time history of the fluctuating inflow at $U_m = 6$ for, (a) '*Type A*' inflow (simulated auto-correlation function depicting the correlation length is shown in (d)), (b) '*Type B*' inflow (simulated auto-correlation function is shown in (e)), and (c) '*Type C*' inflow (simulated auto-correlation function is shown in (f)).

such that the M value varies from 0.3 to 0.5 as the corresponding Mach number dependent empirical parameter values are available in the literature [35]. Note that the Mach number dependent parameters at intermediate values are estimated using the cubic Hermite interpolation technique. Due to the lack of suitable literature under stochastic inflow to compare, the validity of the solver is tested by comparing the C_m vs. α hysteresis plot with those obtained for deterministic inflow case at $M = 0.3$, 0.4, and 0.5. The idea behind this is that, if the hysteresis plot for the stochastic case is in qualitative and quantitative agreement with the individual deterministic cases, the model can be considered valid for the given conditions. Accordingly, it is observed in Fig. 4(b) that the hysteresis plot for fluctuating flow case matches qualitatively with the deterministic cases and is observed to be bounded between the hysteresis plots for $M = 0.3$ and 0.5 cases, respectively. Hence, the present modeling framework is considered valid even under the stochastic inflow.

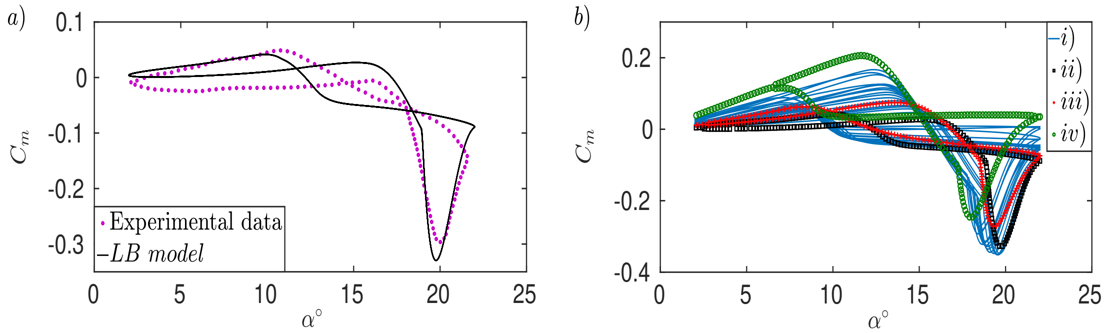

Figure 4: Validation of the LB model in the deterministic and stochastic flow conditions- C_m vs α hysteresis of an airfoil pitching sinusoidally with kinematics : $\alpha(\tau) = 12 + 10\sin(\kappa\tau)$ at $\kappa = 0.0976$, (a) The efficacy of the LB model is established by comparing the C_m vs α hysteresis curves with experimental data [38] at $M = 0.3$, (b) The hysteresis plots under deterministic flow condition at $M = 0.3$, 0.4 and 0.5 (ii, iii, and iv, respectively) obtained using the LB model, are compared with the hysteresis plot under stochastic flow (i) for mean $M = 0.4$, with the $M(\tau)$ randomly fluctuating between 0.3 - 0.5.

2.6. Overview of the rainflow counting algorithm

In order to estimate the fatigue damage from the aeroelastic response, RFC is employed in the present study. The details of this algorithm are briefly presented in this subsection. Under stochastic input flow conditions, the noise-induced aeroelastic responses give rise to random stress cycles. Analysis of random stress cycles are done either in frequency domain or in time domain. Time-domain-based techniques include cycle counting methods such as level crossing, range counting, and RFC [39]. In the level crossing method, only the peak loads above a set limit are counted, and others are neglected, while in range counting, the peak and valley of each load cycle are counted to calculate the strength loss after each cycle. However, these approaches result in erroneous fatigue life predictions in certain cases, particularly where load cycles consist of a combination of low and high amplitude cycles [39]. RFC, despite not accounting for the sequence of load cycles, is the most accurate and most widely used method for estimating fatigue damage in most of the engineering applications [39].

The earliest RFC algorithm was developed by Matsuishi and Endo [40] and was named after the analogy that raindrops are falling from the surface of vertically drawn stress cycles, analogous to the 'pagoda roof'. Over the years, different RFC algorithms were developed, and some of them are listed in [41, 42]. Rychlik[32] gave a new definition of RFC which is illustrated in Fig. 5. This definition involves finding the largest minima L_k on both sides (t^+ and t^-) of each local maxima (H_k), between those local maxima (H_k) and the adjacent higher peaks on both sides. Between the two minima $L_k(t^+)$ and $L_k(t^-)$, the one that corresponds to the minimum downward excursion is defined as k^{th} rainflow minima. The RFC amplitude for k^{th} cycle is thus defined as $(H_k - L_k^{RFC})$.

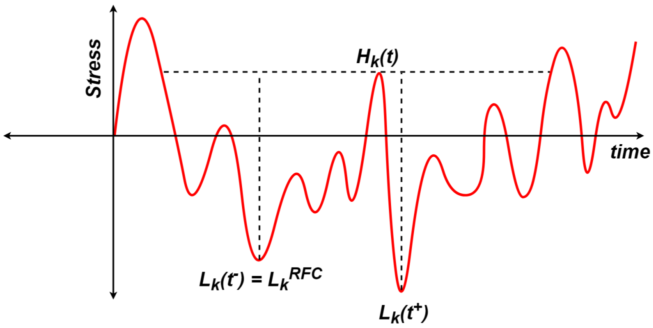

Figure 5: Schematic representation of a typical RFC algorithm [32].

To calculate the fatigue damage, a cycle counting rule is typically integrated with a damage rule. Most widely accepted damage theories are linear accumulation theory given by Palmgren [34], French's endurance-based theory [43] and Langer's two-stage damage based approach [44]. A review of all the popular fatigue damage methods can be found in Fatemi *et al.*[45]. Although endurance strength and two-stage-based techniques are much more detailed, the process is computationally expensive [46]. On the other hand, the linear accumulation theory given by Palmgren is more popular, particularly for comparative studies of fatigue damage among different models [22, 19], due to its simplicity and can be combined effectively with the RFC algorithm.

Based on Palmgren's theory, Miner[33] derived a mathematical model called the linear damage accumulation rule (LDAR) given as $fd = \sum_{n=1}^{k} (n_i/N_i)$, where n_i is the number of load cycles corresponding to i^{th} load level, N_i is the number of load cycles to fail at that level and k is total number of load levels. LDAR is a robust methodology for estimating the fatigue damage based on the assumption of constant energy absorption associated with each cycle [45]. If the net fatigue damage value (fd) approaches unity, it implies that the structure has failed.

3. Numerical aeroelastic response analysis

The present study aims to investigate the dynamical characteristics of a canonical pitch-plunge aeroelastic system subjected to deterministic and stochastic inflows. The response dynamics is compared among linear and nonlinear structural stiffness cases under attached flow (linear) and dynamic stall (nonlinear) conditions. Next, the stresses developed in the structure due to aeroelastic oscillations and the resulting fatigue damage accumulated in the structure are estimated. This section deals with the analysis of the response dynamics of the system. To that end, the state-space form of the coupled governing equations in terms of first-order ODEs are solved using the fourth-order Runge-Kutta numerical integration technique with increasing mean flow speed. An adaptive time-stepping with a tolerance (both absolute and relative) of $\mathcal{O}(10^{-6})$ is used for the deterministic inflow case. On the other hand, a fixed time step of 10^{-4} is chosen through a time step independence test to acquire the numerical solutions for the stochastic inflow case, ensuring the stability of the numerical integration scheme. The nondimensional structural parameters are chosen from Lee *et al.*[3] and are given in Table 1. To incorporate the structural nonlinearity, a cubic nonlinear stiffness in the pitch DoF with $\beta_\alpha = 5$ is chosen for this study. Each case for deterministic or stochastic inflow under attached flow and dynamic stall regimes is simulated for τ = 0-8000, and the time responses are presented in the following subsections. Note that the average simulation time for each deterministic case under isolated structural nonlinearity is approximately 30s, and under aerodynamic/coupled structural-aerodynamic nonlinearity is approximately 3000s. For solutions of each stochastic case under pure structural nonlinearity, computation time is approximately 1500s, and for pure aerodynamic nonlinearity and combined structural/aerodynamic nonlinearity, it is approximately 36000s. The present simulations are performed on a workstation configured with an Intel® Core™ i7-9700 CPU @ 3.00GHz - 8 processors and 64 GB RAM.

Table 1: The nondimensional structural parameters of the aeroelastic system [3].

μ	r_α	x_α	a_h	ϖ
100	0.5	0.25	-0.5	0.2

3.1. Structural responses under deterministic flow conditions

This subsection focuses on investigating the system response under deterministic flow scenarios. First, the sole effects of isolated structural and aerodynamic nonlinearities on the responses signatures are studied. To that end, the structure is considered to possess a cubic nonlinear stiffness in pitch DoF under attached (linear) flow conditions. The unsteady linear formulation based on Wagner's function is used to model the aerodynamic loads in this regime. The bifurcation plot with U as the control parameter is shown in Fig. 6(a). It is observed that the system response transitions from a fixed point to LCO response at $U = 6.25$, beyond which the amplitude of LCOs increases gradually, characterized by the occurrence of a super-critical Hopf bifurcation [3].

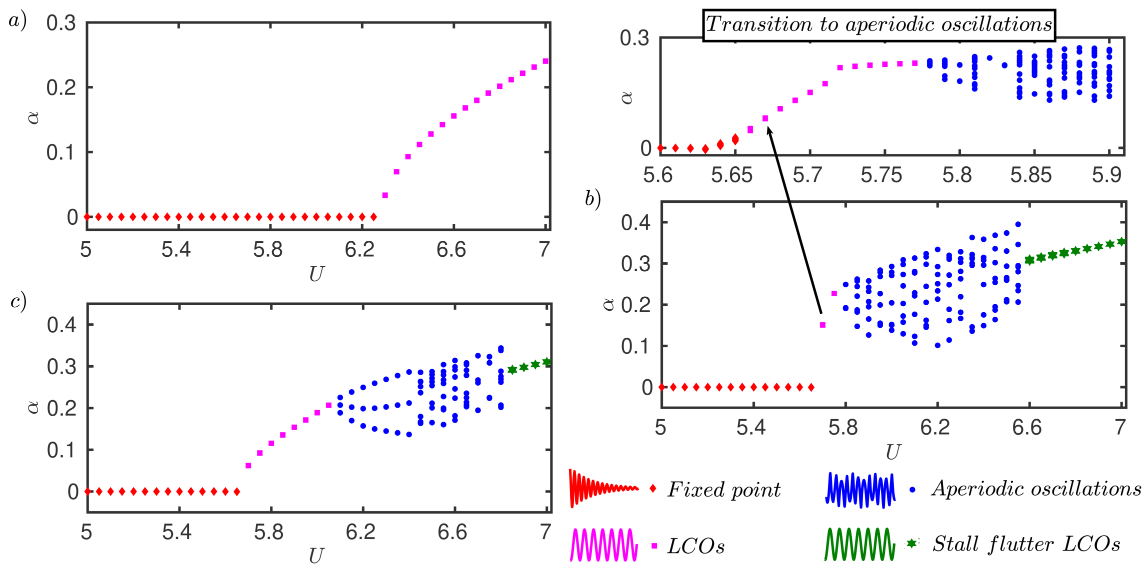

Figure 6: Bifurcation diagrams of pitch response considering the flow speed as the control parameter for (a) nonlinear structure and linear aerodynamics, (b) linear structure and nonlinear aerodynamics, and (c) both nonlinear structure and aerodynamics.

Next, the response dynamics of a linear structure (*i.e.*, $\beta_\alpha = 0$ in Eq. 2), subjected to dynamic stall conditions are studied using the LB model to investigate the isolated effects of aerodynamic nonlinearity. It is observed in Fig. 6(b) that the onset of LCOs occurs at $U = 5.65$, which then transition into aperiodic responses at $U = 5.8$. A zoomed view of the responses between $U = 5.6$-5.9 is also presented in Fig. 6(b), showing the transition from fixed point to aperiodic oscillations via an LCO regime. The onset of aperiodicity marks the first occurrence of a dynamic stall event, which is evident from the x_9 - x_{10} and α - α' phase plots (see Fig. 7). Dynamic stall phenomenon in LB model is characterized by the discontinuous boundaries present at $x_9 = \pm C_{n1}$ (onset of stall/ flow reattachment) and $x_{10} = 0.7$ (dynamic trailing edge separation point corresponding to static stall angle). Note that x_9 and x_{10} represent the state values of the LB model and details of the same can be found in our recent work [14]. Fig. 7(a) shows that the flow remains attached at $U = 5.66$, as the x_9 and x_{10} values do not cross the discontinuity boundaries. At $U = 5.79$, value of x_9 crosses $\pm C_{n1}$ and x_{10} approaches 0.3, indicating that the trailing edge separation point lies at $0.3c$ from the leading edge and the response dynamics switches aperiodically between deep and light dynamic stall events (Fig. 7(b)). Note that light stall regime corresponds to amplitude of oscillations reaching static stall angle-of-attack which lies closely to the AoA at $x_{10} = 0.7$ and deep stall regimes lie beyond light stall regimes, where a large vortex spends significant time on the airfoil surface before shedding. The aperiodic nature of the responses at $U = 5.79$ is further substantiated by the α - α' phase portrait shown in Fig. 7(e). As U reaches 6.6, x_9 - x_{10} phase portrait (see Fig. 7(c)) shows that the dynamics enter into deep stall event completely and the response signature becomes periodic, marking the onset of stall flutter LCOs (see Fig. 7(f)).

Next, the combined effect of structural cubic hardening nonlinearity and aerodynamic nonlinearity governed by dynamic stall on the system responses is investigated. The bifurcation plot for the same is provided in Fig. 6(c). It is observed that the onset of flutter instability occurs almost at the same flow speed ($U = 5.65$) as in the case of isolated aerodynamic nonlinearity (see Fig. 6(b)). It is worth noting that the bifurcation point has shifted to lower flow speed as compared to the system with isolated structural nonlinearity. This may be attributed to the LB model's capability of accounting for the nonlinear effects from the flow (wake effects from flow separation and accounting for compressibility). Therefore, it is conjectured that the presence of nonlinearities in flow advances the bifurcation onset in the response signatures. Furthermore, the LCOs occurring post-bifurcation span over a larger flow speed regime, and the transition to aperiodic responses (at $U = 6.45$) from LCOs occurs via a short regime of period-3 oscillations between $U = 6.1$-6.4. The onset of large-amplitude stall flutter LCOs is observed to be postponed to $U = 6.8$ as compared to $U = 6.6$ in the case of a system with isolated aerodynamic nonlinearity (see Fig. 6(b)).

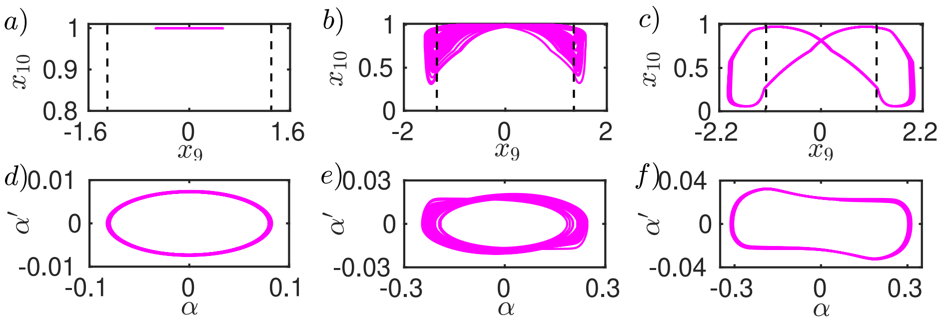

Figure 7: x_9 - x_{10} phase portrait (a) at $U = 5.66$, corresponding to the onset of LCOs, (b) at $U = 5.79$, showing the transition of LCOs to aperiodic oscillations and (c) at $U = 6.6$, corresponding to the stall flutter oscillations. The dashed lines in (a-c) indicate $\pm C_{n1}$. The α - α' phase portrait of the response signatures at (d) $U = 5.66$, (e) $U = 5.79$ and (f) $U = 6.6$.

So far, the bifurcation scenarios in the deterministic aeroelastic system with isolated nonlinearity either in the structure or flow, followed by combined nonlinearities are presented. Equipped with this insight, we repeat this exercise for the nonlinear aeroelastic system subjected to randomly fluctuating input wind in the next subsection.

3.2. Structural responses under stochastic flow conditions

In this part, the time responses of the system with isolated nonlinearity in structure and flow are obtained first, followed by an investigation into the effect of coupled nonlinearities on system responses under stochastic flow conditions achieved by randomly varying the inlet velocity about a mean value of (U_m). It is worthwhile to mention that bifurcation diagrams cannot be explicitly presented in the stochastic case - as found in Fig. 6. Indeed, one needs to invoke the concepts of stochastic bifurcations via the evolution of probability density function, and/or estimate Lyapunov exponents, and/or estimate Shannon entropy as elaborated in Venkatramani *et al.* [26]. Doing the same is beyond the scope of objectives entailing in the present study. Therefore, we restrict our discussions by merely presenting the time histories of the responses and use visual inspection to discern the qualitative nature of the stochastic aeroelastic responses (in lines with [25]). Recalling the discussions in Sec. 2.4, three different types of fluctuating inflow, involving different time scales - defined as '*Type A*', '*Type B*' and '*Type C*' are considered in this study with various noise intensities ranging from 0.1 to 0.3. It is to be noted that only selected cases representative of notable transitions impacting structural safety are discussed in this paper for the sake of brevity.

Fluctuating inflow imposed upon structure possessing pitch cubic hardening nonlinearity under attached flow condition is observed to significantly alter the response dynamics of the system (see Fig. 8) and is consistent with the observations reported hitherto [47, 26]. The time scale of the flow, on the other hand, is observed to play a major role in defining the qualitative nature of the response characteristics. Therefore, as a starting step, a larger emphasis is placed on demarcating the response dynamics at different time scales at a constant value of $\sigma = 0.3$. Subsequently, the effect of different σ values on the system response is investigated in this study and is presented in the later part of this subsection.

Under '*Type A*' inflow (corresponding to a short time scale), the pitch response at $U_m = 5.6$ decays to a fixed point (see Fig. 8(a)) and at $U_m = 6$, a transient "burst" of oscillations appear which then switch to a fixed point signature; see Fig. 8(b). At $U_m = 6.6$, large-amplitude LCOs with random variations in the amplitude are observed; see Fig. 8(c). Finally at $U_m = 7$, response transitions to well developed random LCOs; see Fig. 8(d). Note that the intermittency route to random LCOs presented here are consistent with the observations of Venkatramani *et al.* [25, 26, 27].

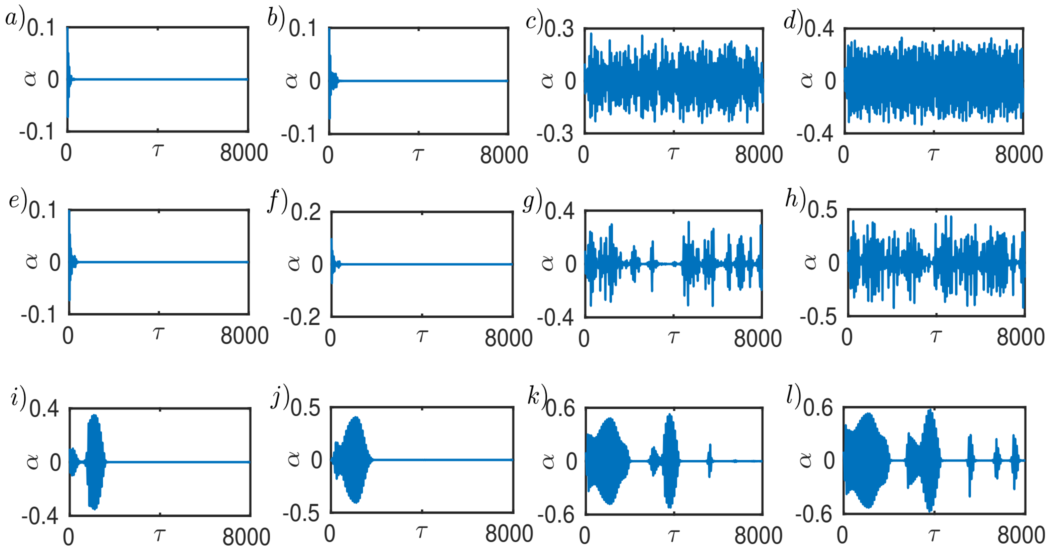

Figure 8: Pitch responses of system possessing structural nonlinearity under attached flow conditions subjected to stochastic inflow conditions with $\sigma = 0.3$; for '*Type A*' inflow at (a) $U_m = 5.6$, (b) $U_m = 6$, (c) $U_m = 6.6$, and (d) $U_m = 7$; for '*Type B*' inflow at (e) $U_m = 5.6$, (f) $U_m = 6$, (g) $U_m = 6.6$, and (h) $U_m = 7$; and for '*Type C*' flow at (i) $U_m = 5.6$, (j) $U_m = 6$, (k) $U_m = 6.6$, and (l) $U_m = 7$. The pitch angle presented throughout the manuscript are in radians.

Under '*Type B*' fluctuating inflow, involving a time scale slightly larger than the system time scale, the system responses at $U_m = 5$ and $U_m = 6$ are seen to be similar to those observed for the '*Type A*' inflow (see Fig. 8(e) and Fig. 8(f)). However, as U_m is increased, the time responses are observed to possess sporadic bursts of periodic oscillations switching intermittently with low amplitude oscillations or rest/off regimes (see Fig. 8(g) and Fig. 8(h)). This is indicative of "burst-type" intermittency [25]. It is to be cautioned that '*Type B*' input flow possesses a time scale only marginally higher than the system time scale and can be perhaps defined as input flows with "moderate" time scales. Venkatramani *et al.* [25] on the other hand, used isolated cases of extremely short time scale input flows (wherein the correlation time of the random input wind is very short compared to the system time scale) and reported regimes of intermittent periodic oscillations amidst low-amplitude aperiodic oscillations - which was termed to be "burst" type intermittency in aeroelastic responses. One needs to be mindful of the distinct correlation structure found in the '*Type B*' fluctuating inflow and thereby in interpreting the responses presented in Figs. 8(g) and 8(h) as "burst" type intermittency. Studies on the correlation structure of the random input process, hand-in-hand with the noise characteristics [48] have shown that the genre of noise-induced intermittency in dynamical systems needs closer attention in attributing terminologies. Nevertheless, given that the present work is focused on utilizing the stochastic aeroelastic responses to compute the fatigue damage, carrying out investigations into the genres of noise-induced intermittent aeroelastic responses will be beyond this study.

Under '*Type C*' flows (see Figs. 8(i) - 8(l)), involving a long time scale, one observes sporadic periodic oscillations at lower values of U_m, which eventually gives away to a decaying signature. As U_m increases, periodic oscillations ("on" state) are found interspersed amidst segments of decaying signatures ("off" state), and thereby called noise-induced "on-off" intermittency. The time responses presented in Fig. 8 are consistent with the findings presented in [47, 25, 27]. It is worth noting that the responses presented in Fig. 8 for flows characterized as '*Type B*' and '*Type C*' transition to random LCOs for larger values of U_m. However, for reasons described in the next part involving dynamic stall, we refrained from showing the eventual culmination of intermittent responses into random LCOs.

Next, we turn our attention to the response dynamics of the system with only aerodynamic nonlinearity under randomly fluctuating flow conditions with different time scales. In this case, the amplitude of the pitch response is much higher than those obtained for isolated structural nonlinearity. The qualitative nature of the pitch responses here as well shows different intermittent signatures under different time scales. For the '*Type A*' inflow, one observes a fixed point response for low values of U_m that transforms itself into fully developed LCOs at higher values of U_m; see Figs. 9(a)-(d). Though "burst" type intermittency is observed at intermediate values of U_m, we have refrained from explicitly presenting them here to maintain consistency in the U_m values used throughout this manuscript. The "burst" type intermittency route to fully developed LCOs are shown for the '*Type B*' inflow; see Figs. 9(e)-(h). In accordance with using a long time scale input flow, 'on-off' intermittent behavior is observed under '*Type C*' inflow for U_m = 6-7 (see Fig. 9(j), Fig. 9(k) and Fig. 9(l)). The amplitude of the 'on' states increases gradually with the mean flow speed and eventually transforms into LCOs. Note that though the LCOs are observed in higher values of U_m, we have refrained from presenting them here. This is so because the aerodynamic forces modeled via the LB formulation are *acceptable* and *accurate* for restrictive values of α [31, 1, 13]. Indeed, the availability of experimental parameters needed for the LB model is usually well available for $\alpha < 40^\circ$ (≈ 0.7 radians) [13]. Therefore, though in line with the hitherto studies [25, 14], an intermittency route to LCO is encountered in the present case, the accuracy of the responses once $\alpha > 40^\circ$ becomes a concern. In turn, we avoid presenting the responses obtained at higher values of U_m. Given the need to compare the time histories of the responses, and correspondingly, the accumulated fatigue damage; the LCOs obtained even from unsteady aerodynamic formulations at higher values of U_m are not presented earlier in Fig. 8.

Next, the time responses corresponding to the system possessing both structural and aerodynamic nonlinearities (coupled nonlinearities) are obtained and shown in Fig. 10. From visual inspection, it is evident that the aeroelastic responses obtained from the system with coupled nonlinearities are qualitatively similar to the responses of a system with a linear structure subjected to nonlinear aerodynamic loads (see Fig. 9). The responses are also found to be consistent with the findings from [14]. However, the amplitude of responses is observed to be reduced with the inclusion of a cubic hardening nonlinearity in the structural stiffness behavior, as compared to the system responses under pure aerodynamic nonlinearity reported in Fig. 9.

It is worth reiterating that the presented aeroelastic dynamics are stochastic and nonlinear.

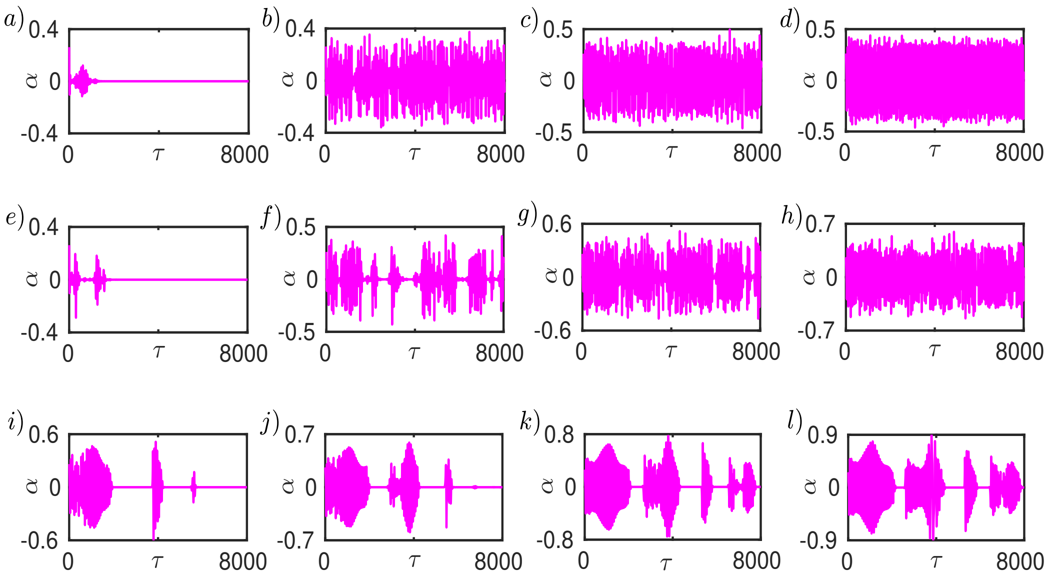

Figure 9: Pitch responses of system with linear structure under nonlinear flow conditions subjected to stochastic inflow conditions with $\sigma = 0.3$; for '*Type A*' inflow at (a) $U_m = 5.6$, (b) $U_m = 6$, (c) $U_m = 6.6$, and (d) $U_m = 7$; for '*Type B*' inflow at (e) $U_m = 5.6$, (f) $U_m = 6$, (g) $U_m = 6.6$, and (h) $U_m = 7$; and for '*Type C*' inflow at (i) $U_m = 5.6$, (j) $U_m = 6$, (k) $U_m = 6.6$, and (l) $U_m = 7$.

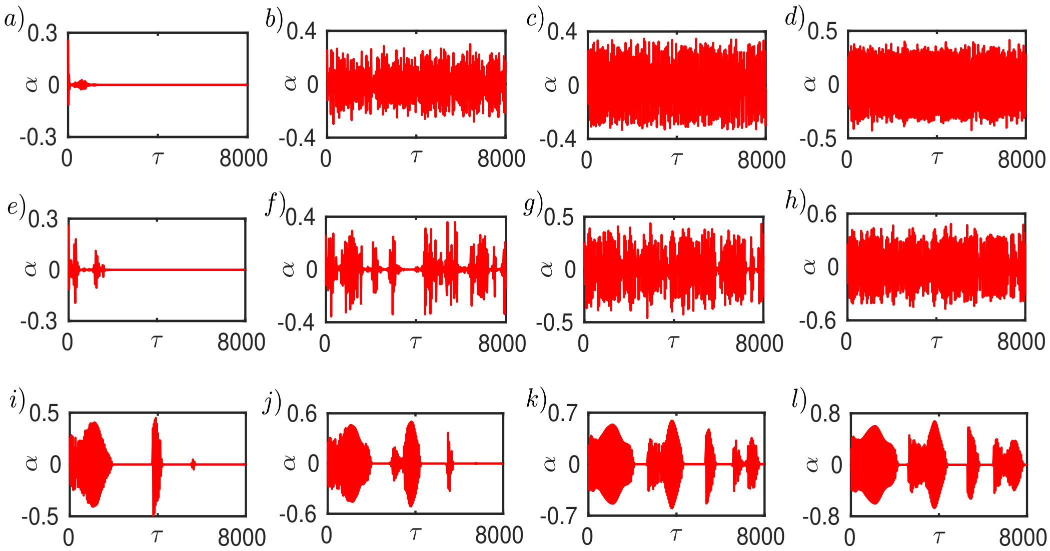

Figure 10: Pitch responses of system with nonlinear structural stiffness behavior under nonlinear flow conditions subjected to stochastic inflow conditions with $\sigma = 0.3$; for '*Type A*' inflow at (a) $U_m = 5.6$, (b) $U_m = 6$, (c) $U_m = 6.6$, and (d) $U_m = 7$; for '*Type B*' inflow at (e) $U_m = 5.6$, (f) $U_m = 6$, (g) $U_m = 6.6$, and (h) $U_m = 7$; and for '*Type C*' flow at (i) $U_m = 5.6$, (j) $U_m = 6$, (k) $U_m = 6.6$, and (l) $U_m = 7$.

In other words, the qualitative and quantitative characteristics are dictated by the genres of the nonlinearity (type, location, and strength of the nonlinearity) and genres of the random input flow (noise intensity, time scales, and probabilistic distributions). Given the goal of this work to hand-in-hand characterize the incurred fatigue damage against the dynamical signature, a brief attempt to characterize the time responses by varying the noise intensity of '*Type A*', '*Type B*' and '*Type C*' inflow fluctuations are presented next. It is to be cautioned to the reader that though '*Type A - Type C*' inflow have different time scales, a change in the noise intensity can affect the time scale of the random process as well [25, 26]. Disregarding the interdependence of the time scale and noise intensity of the random process, for the ease of mathematical modeling, we present the aeroelastic response dynamics by merely varying the noise intensity σ and assume that this exercise has no considerable impact on the time scales of '*Type A - Type C*' inflow. Another important probabilistic marker that can considerably affect the signature of the aeroelastic responses, and in turn, the structural safety/fatigue damage accumulation, is the probability distribution of the input random wind. Recall that in Eq. 12, $U(\tau)$ is assumed to be a Gaussian random process. Introduction of non-Gaussian distributions and investigating the aeroelastic dynamics along with the fatigue analysis are rife with computational challenges and would demand a separate study.

Accordingly, fixing $U_m = 6.6$, we present three cases of noise intensity (namely, $\sigma = 0.1, 0.2$ and 0.3) for the flows represented via '*Type A - Type C*'; see Fig. 11. For the '*Type A*' inflow case, representing the short time flow fluctuations, one observes that an increase in the noise intensity augments the random variations in the peak amplitudes of the LCOs and is akin to that reported in [26]. In the '*Type B*' case, an increase in the noise intensity transforms the sustained LCOs into a "burst" type intermittency, albeit with minimal presence of the aperiodic oscillations. As elaborated in Krishna *et al.* [48], without a hand-in-hand analytical knowledge of the noise intensity, time scale, and the probabilistic distributions, it would be premature to comment on the genre of the intermittency as well as the extent of *laminarity length* (which dictates the duration of aperiodic fluctuations). Interestingly, increasing the noise intensity to 0.3 transforms the response dynamics into a visibly evident "burst" intermittency - indicating a delayed onset of LCOs [26] - which in turn can affect the accumulated fatigue damage. This will be taken up in the next part. For the '*Type C*' flow case, corresponding to long time scale flow fluctuations, it is observed that despite an increase in the noise intensity from 0.1 to 0.3, the "on-off" type intermittency is consistently observed; albeit with varying laminarity length. Random LCOs are not captured, perhaps due to a considerable shift in its onset [25]. Indeed, the appearance of "on-off" type intermittency and its culmination into sustained LCOs depends on the flow speed remaining above or below the critical limit for a sufficient duration of time; refer to Venkatramani *et al.* [25] for detailed discussions on the same for a stochastic classical flutter system.

To demonstrate the same for the present aeroelastic system, we show the variations of $U(\tau)$ versus τ for the '*Type C*' flow in Fig. 12. At lower intensity of fluctuations, $U(\tau)$ fluctuates continuously above the critical flow speed U_{cr} (see Fig. 12(a)). Consequently, the corresponding aeroelastic response is a sustained LCO; see Fig. 12(d). Increasing σ, $U(\tau)$ fluctuates above and below U_m (see Fig. 12(b)) and correspondingly giving rise to "on-off" type intermittency in the aeroelastic response; see Fig. 12(e). This trend is observed even when the noise intensity becomes 0.3 (see Fig. 12(c)). However, the extent of time it stays above and below the critical speed is different owing to the changed noise intensity. As discussed earlier, the time scale and intensity of fluctuations dictate this mapping between the randomness in the input flow and the noise-induced "on-off" intermittency in the output dynamics [48].

So far, it is observed that nonlinearity arising from structure and flow has different effects on system dynamics under deterministic conditions. Structural nonlinearity restricts the divergent oscillations to LCOs beyond the critical flutter boundary under the assumption of the attached wake. Under aerodynamic nonlinearity, structure manifests phenomenologically richer dynamic responses governed by flow separation and reattachment. On the other hand, time scales and noise intensity of the fluctuating inflow are crucial in determining aeroelastic responses under stochastic conditions. At this interim juncture we note the following.

- Based on the time-scales of the input flow fluctuations, one can either encounter "on-off" type or "burst" type intermittent behavior.

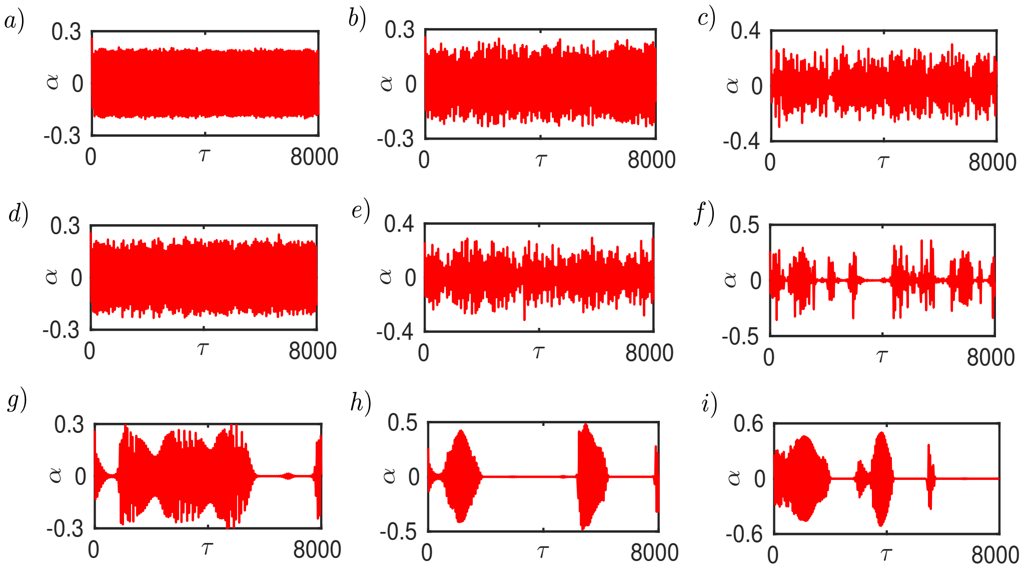

Figure 11: Effect of intensity of fluctuating inflow on aeroelastic responses at $U_m = 6$ under nonlinear aerodynamic loads and nonlinear structure; time histories with '*Type A*' inflow for, (a) $\sigma = 0.1$, (b) $\sigma = 0.2$, and (c) $\sigma = 0.3$; time histories with '*Type B*' inflow for, (d) $\sigma = 0.1$, (e) $\sigma = 0.2$, and (f) $\sigma = 0.3$; time histories with '*Type C*' inflow for, (g) $\sigma = 0.1$, (h) $\sigma = 0.2$, and (i) $\sigma = 0.3$.

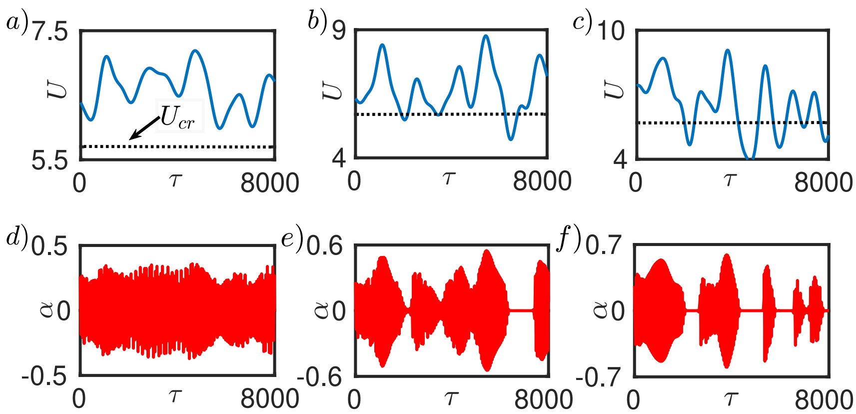

Figure 12: Effect of intensity of fluctuating inflow on aeroelastic responses at $U_m = 6.6$ for '*Type C*' inflow under nonlinear aerodynamic loads and nonlinear structure. Time histories of '*Type C*' inflow at $U_m = 6.6$ for, (a) $\sigma = 0.1$, (b) $\sigma = 0.2$, and (c) $\sigma = 0.3$; and corresponding pitch responses for (d) $\sigma = 0.1$, (e) $\sigma = 0.2$, and (f) $\sigma = 0.3$, respectively. The critical flutter velocity (U_{cr}) is 5.65 and shown by dashed lines.

- If the input wind fluctuates with predominantly long time scales, the aeroelastic dynamics switches between high-amplitude periodic oscillations called "on" states, and states of decayed oscillations called "off" states. A hand-in-hand increase in noise intensity of the flow fluctuations result in increased switching between the "on" and "off" states.
- If the input wind fluctuates with predominantly short time scales, the dynamics of the airfoil displays near random switching between states of periodic oscillations interspersed amidst states of aperiodic oscillations. As observed in [26], an increase in fluctuation intensity yields in an easier hopping of trajectories from one attractor to another, leading to unpredictable stitching's in the intermittent dynamics. In otherwise, the average laminarity length of the noise-induced intermittency in our considered stall flutter system gets altered [48].

It is worth reiterating that though few studies on stochastic stall flutter systems exist hitherto [22, 15, 14], minimal attempts have been made to characterize the noise-induced transitions in the route to stochastic stall flutter. Consequently, the impact of probabilistic markers like time scales of the input fluctuating flow, and its noise intensities over the nature of the response dynamics has remained largely unexplored. The present study makes its first end of contribution by presenting the noise-induced intermittency as an intermediate stage of oscillations that can ultimately culminate into torsionally dominant random LCOs (stochastic stall flutter). Indeed, one observes that numerous studies on engineering that encountered noise-indudced intermittency have taken elaborate steps to develop measures that can predict both (i) transitions to intermittency from state of low amplitude oscillations [49, 50, 51] and (ii) transitions from intermittency to large amplitude LCOs [52, 53], underscoring the need for structural safety assessment. For the considered stochastic stall problem, we address this end of specific concern in the next section. For the sake of comparison, we compare the fatigue damages incurred in classical flutter systems as found in [19].

4. Fatigue damage analysis

Complex dynamical signatures in stochastic nonlinear aeroelastic systems can presumably induce a considerable amount of fatigue damage in the aeroelastic structures. Indeed, one can conjecture that repeating time histories (of different patterns) can give rise to complex stress cycle reversal and fatigue damage to the aeroelastic system. Unlike the failure that occurs through the first passage of time, fatigue damage accumulation is usually not noticed until the appearance of fatigue cracks, which can rapidly propagate towards a fracture failure. Noting that the development of fatigue failure can be more rampant in the vicinity of LCOs, Venkatramani *et al.* [26] developed a suite of measures that can foretell an impending flutter in a stochastic aeroelastic system with cubic stiffness nonlinearity, and thereby changing the operating conditions to dissuade the onset of this instability. The present study deals with far more complex nonlinearities and fluctuating flow parameters, thereby giving rise to various dynamics and random LCOs. The accumulation of fatigue damage in these corresponding response dynamics and the augmenting role of nonlinearities and randomness in the input flow remains undocumented in the hitherto literature. Addressing this issue is a focal objective of this study, and the methodology to do the same are elucidated next.

The aeroelastic system is assumed to be a cantilever beam of 20 m length and uniform cross-section. Although the loading on wings and blades under fluid-structure interaction is complex, a uniformly distributed loading is considered here. The cross-section is taken as a NACA 0012 airfoil with a cord length of 0.61 m. Here, only pitch-plunge responses obtained for a 2-DoF reduced-order model are used to obtain stresses in a 3D aeroelastic structure- akin to that in Venkatesh *et al.* [19].

The airfoil is subjected to multi-axial loading, bending stress due to plunging motion, and torsional stress due to pitching motion. To convert the state of stress from multi-axial to uniaxial, signed von Mises criteria given by Bracessi *et al.*[54] is implemented. Signed von Mises criterion possesses sudden jumps associated with stress reversal, and yet owing to its ease of computing the damage accumulation - one resorts to using this criterion. The airfoil material is assumed to be isotropic, composed of aluminum alloy *Al* 6082-*T*6, having modulus of elasticity $(E) = 70$ GPa, shear modulus $(G) = 26.4$ GPa and yield strength 250 MPa and is same as that provided in [19]. Under reversible loading, $S-N$ characteristics or stress amplitude (S) vs number of cycles to failure (N) relationship for *Al* 6082-*T*6 are experimentally obtained by Carpinteri *et al.* [55]. Under reversible bending

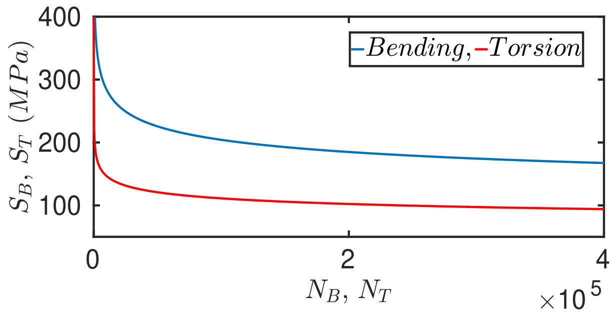

Figure 13: S-N curves for the material for bending and torsional stress.

stresses, $S_B = 1067 \times {N_B}^{0.1436}$ and under reversible torsional stresses, $S_T = 446.3 \times {N_T}^{0.1207}$, where S_B and S_T are reversible bending and torsional stress amplitudes, respectively, and N_B and N_T are the number of cycles to fail under S_B and S_T, respectively.

Due to plunge motions, normal bending stresses will be developed, proportional to the displacement (y) of the section above the neutral axis. Additionally, there will be a net shear force and hence shear stress in the y-direction. However, the magnitude of the shear stresses due to bending is observed to be inconsiderable as compared to normal bending stresses, which is also shown in [19]. Hence, only normal bending stresses are taken into consideration here. From the theory of simple bending, bending stress is given as $\sigma_{zz} = (M_b/I)y$, where M_b is the bending moment, and I is the area moment of inertia of the airfoil cross-section about the x-axis. The stresses will be highest at the maximum thickness or y_{max}.

Calculation of torsional stresses due to pitching motion is rather complicated to evaluate as warping is a significant factor due to non-circular cross-section. Due to warping, there will be out of plane displacement also (i.e., in the z-direction), which will be proportional to the rate of twist θ and a function $\psi(x, y)$, such that $\Delta z = \theta\psi(x, y)$. The product $z\theta$ is the rotation of the cross section at z distance and is obtained from pitch time histories. All direct strains and shear strain in x-y plane are zero and hence corresponding stresses are also zero. Remaining two shear strains (γ_{zx}) and (γ_{zy}) are given as [19],

$$\gamma_{zx} = \theta\left(\frac{\partial\psi}{\partial x} - y\right), \qquad \gamma_{zy} = \theta\left(\frac{\partial\psi}{\partial y} + x\right). \tag{15}$$

The corresponding shear stresses are given as $\sigma_{zx} = G\gamma_{zx}$ and $\sigma_{zy} = G\gamma_{zy}$. Consequently,

$$\frac{\partial\sigma_{zy}}{\partial x} - \frac{\partial\sigma_{zx}}{\partial y} = 2G\theta. \tag{16}$$

A stress function called Prandtl stress function (ϕ) is now introduced such that, $\sigma_{zx} = \partial\phi/\partial y$ and $\sigma_{zy} = -\partial\phi/\partial x$. Substituting (ϕ) into Eq. 16, we obtain

$$\frac{\partial^2\phi}{\partial y^2} + \frac{\partial^2\phi}{\partial x^2} = -2G\theta. \tag{17}$$

For a symmetric airfoil such as NACA 0012, the cross section is given as, $y = a\zeta\,(x/c)$ and $y = -a_1\zeta\,(x/c)$, where $\zeta\,(x/c) = (x/c)^{m_1}\,[1 - (x/c)^{p_1}]^{q_1}$. The value of stress function ϕ for a symmetric airfoil section is given as

$$\phi = A(y - a\zeta)(y + a_1\zeta), \tag{18}$$

where $A = -G\theta/[1 + (\alpha_1/c^2)(a^2 + {a_1}^2 + aa_1)]$ and the parameters a, a_1, p_1, q_1, m_1 and α_1 are constants for a particular airfoil cross section. For a NACA 0012 airfoil section, the parameters are obtained as $a = 0.94$, $a_1 = 0.94$, $p_1 = 0.139$, $q_1 = 1$, $m_1 = 0.75$, $\alpha_1 = 0.0083$. More details of stress calculations and NACA 0012 parameters can be found in [19].

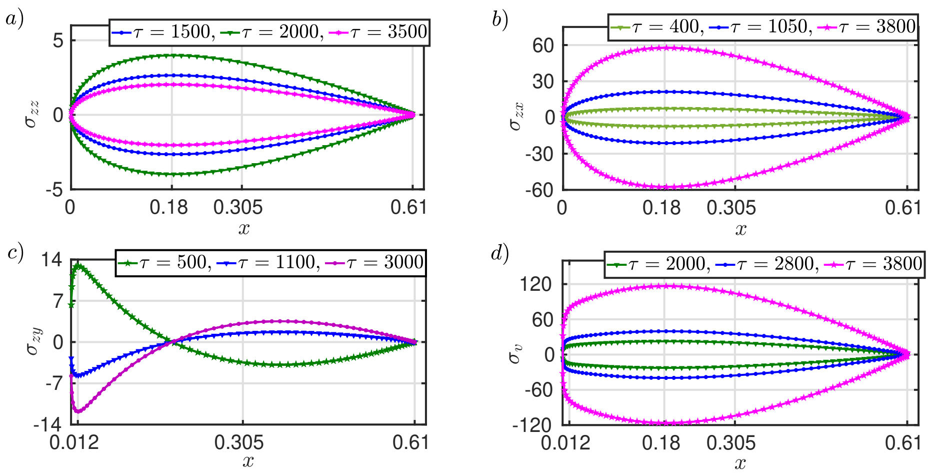

Figure 14: Variation of (a) σ_{zz}, (b) σ_{zx}, (c) σ_{zy}, and (d) σ_v, along the chord length x (meters). All the stresses are in MPa.

Since both torsional and bending stresses act simultaneously, the loading is multiaxial. An approximate method to convert the multiaxial stresses to a uniaxial state of stress, 'signed von Mises criterion' is implemented here, which is given as,

$$\sigma_v = \sqrt{\frac{(\sigma_{xx} - \sigma_{yy})^2 + (\sigma_{yy} - \sigma_{zz})^2 + (\sigma_{zz} - \sigma_{xx})^2 + 6({\sigma_{xy}}^2 + {\sigma_{yz}}^2 + {\sigma_{zx}}^2)}{2}}. \tag{19}$$

Here, the sign of the von Mises stress is taken as that of maximum principal stress. Since the system responses are random in nature, obtained time histories of bending stress ($\sigma_{zz}(\tau)$), torsional stresses ($\sigma_{zx}(\tau)$ and $\sigma_{zy}(\tau)$) and von Mises stress ($\sigma_v(\tau)$) are also random. RFC algorithm given by Rychlik [32] is implemented to extract the load levels and turning points from random stress time histories. A MATLAB based 'WAFO toolbox' is utilized to calculate the RFC and corresponding damage values [56] using the Miner's rule [33].

4.1. Estimation of stresses

For fatigue damage analysis, estimation of critical points or the locations of maximum stresses in both bending and torsional modes are required. To that end, bending and torsional stresses are calculated individually at arbitrarily chosen nondimensional time instants along the chord length. It is observed in Fig. 14(a) that σ_{zz} is maximum at $x = 0.18$ m, measured from the leading edge, which corresponds to the location of maximum airfoil thickness ($y = 0.037$ m). σ_{zy} is found to be maximum at $x = 0.012$ m which is a point close to the leading edge (see Fig. 14(b)) and the airfoil thickness at this location is $y = 0.015$ m. σ_{zx} is found to be maximum at $x = 0.18$ m, which again corresponds to the location of maximum thickness of airfoil (see Fig. 14(c)). So, the two critical points on airfoil surface are obtained as ($x = 0.012$ m, $y = 0.015$ m) and ($x = 0.18$ m, y = 0.037 m). Note that the location of critical points do not vary with time.

Next, the concept of signed von Mises stress is invoked to convert the multi-axial state of stress to a uniaxial state. The variation of σ_v along the chord is shown in Fig. 14(d). It is observed that σ_v increase rapidly until a chord length of 0.012 m (the location of maximum σ_{zy} developed) and continues to increase albeit at a slower rate as chord value approaches 0.18 m, which corresponds to the location of maximum thickness. Beyond this location, von Mises stress gradually decreases. Thus, the point located at $x = 0.18$ m, $y = 0.037$ m is susceptible to maximum von Mises stress and treated as the only critical point in this study.

4.1.1. Developed stresses under deterministic flow

Stress time histories are generated under deterministic inflow conditions by calculating the stresses at the critical point. Under deterministic flow, the stress cycles are time-invariant and

Table 2: Stress amplitude (in MPa) of σ_{zz}, σ_{zx}, σ_{zy} and σ_v under deterministic flow conditions.

Aeroelastic model	U	$\sigma_{\mathbf{zz}}$	$\sigma_{\mathbf{zx}}$	$\sigma_{\mathbf{zy}}$	$\sigma_{\mathbf{v}}$
Attached flow/	6.6	3.64	18.11	0.17	29.75
nonlinear structure	7.0	4.81	22.85	0.17	39.53
Nonlinear aerodynamics/	6.6	3.12	28.39	0.20	49.61
linear structure	7.0	2.70	32.20	0.23	55.83
Nonlinear aerodynamics/	6.6	2.64	26.55	0.19	45.8
nonlinear structure	7.0	2.10	28.51	0.20	49.28

have a constant stress amplitude. Amplitudes of bending, torsion, and von Mises stress cycles are shown in Table 2, for $U_m = 6.6$ and 7, respectively. For nonlinear structures under attached flow conditions, stress amplitudes increase with the flow speed. For the other two cases of nonlinearity, all the stress amplitudes are proportional to flow speed except the bending stresses, which is due to high amplitude plunge responses during the aperiodic regime. It is observed that the amplitude of σ_{zy} is almost negligible as compared to that of σ_{zx}. Also, amplitude of σ_{zz} is significantly small as compared to σ_{zx}. Thus, the resultant von Mises stresses are mainly contributed by σ_{zx}. Bending stresses are plunge dominant and found to be highest when the flow is attached and the structure possessing cubic hardening nonlinearity in pitch, which is due to linearity in plunge stiffness. On the other hand, torsional stresses are highest under nonlinear aerodynamics and with linear structure, owing to the pitch dominant oscillations under dynamic stall event [1]. Since σ_{zx} has greater contribution in determining σ_v, as compared to σ_{zz}, the amplitude of σ_v is highest under nonlinear aerodynamics for a linear structure. Incorporating cubic hardening nonlinearity in pitch results in reduced torsional stresses and hence the resulting von Mises stresses also reduce significantly. In field conditions, stress cycles are random. Hence, a more detailed analysis is presented next, in which stresses developed under the fluctuating inflow of different time scales and intensities are analyzed. However, the results obtained under deterministic inflow are important as the isolated effect of different nonlinearities on bending and torsional stresses is explicitly observed.

4.1.2. Developed stresses under stochastic flow

Akin to aeroelastic response analysis, stresses time histories under stochastic flow conditions are obtained for three time scales '*Type A*', '*Type B*' and '*Type C*' at intensity $\sigma = 0.1$, 0.2 and 0.3, at constant intervals of mean flow speeds (U_m) from 5 to 7. It is observed that the maximum amplitudes of resultant random stress cycles are obtained at $U_m = 7$ and $\sigma = 0.3$, which are presented in Table 3 and Fig. 15. Table 3 shows the maximum stress values from the random time histories of σ_{zz}, σ_{zx}, σ_{zy} and σ_v along with the number of RFC. Similar to deterministic inflow conditions, torsional stresses are predominant under stochastic inflow conditions as well. It is noted that stresses developed under stochastic inflow are significantly higher than those under deterministic inflow. It should be noted that the maximum stress values in all the cases are much below the yield strength of the material (250 MPa). Developed stresses are observed to be highest when the structure is linear and nonlinearity is solely aerodynamic, and lowest when the nonlinearity is solely structural. The combined presence of structural nonlinearity into aerodynamic nonlinearity reduces the stress amplitude and requires lesser magnitude stress cycles. It is evident that the longer the time scale, the higher the amplitude of stress cycles. Under '*Type C*' inflow, the stress amplitudes are much higher than those under the other two inflow types. However, there are distinct regimes of zero stress levels as well. On the contrary, '*Type A*' inflow, having the shortest time scale among three cases, gives rise to relatively lower amplitude random stress cycles, but there is no well-defined regime of zero stress levels. Upon estimating the RFC of these stress cycles, it is seen that the shorter the time scale, the higher are the rainflow cycles counts, which means higher the number of load levels. Prediction of relative fatigue damage at different time scales from stress time histories alone is challenging. Therefore, a damage rule has been adopted in section 4.2.

4.2. Fatigue damage estimation

In this section, fatigue damage is obtained using LDAR from resulting von Mises stresses. The RFC algorithm described in subsection 2.6 is used to estimate the number of rainflow cycles from each von Mises stress time history. If t_k be the time of the k^{th} local maxima, corresponding rainflow amplitude for any k^{th} cycle is given as $s_k^{RFC} = H_k - L_k^{RFC}$ (see Fig. 5). The damage at time t is given as [56]

$$fd = K \sum_{t_k \leq t} (s_k^{RFC})^{\beta}. \tag{20}$$

where K and β are material constants, which are estimated from Fig. 13. Damage values are calculated by systematically varying the flow speed under deterministic and stochastic conditions. Since the stochastic inflow is modelled as Gaussian random process, assumption of ergodicity can be considered while calculating the random stresses. It is worth mentioning that all the damage values will numerically vary for different structural and flow parameters as well as for different damage criteria. However, comparative inferences can be drawn from fatigue data to understand the effect of various factors like the type of nonlinearity, flow speed, time scale, and intensity of flow fluctuations on structural damage.

4.2.1. Fatigue damage under deterministic conditions

Under deterministic conditions, the damage is estimated for nondimensional flow speed U = 5-7 for three nonlinear models undertaken in the present study and are presented in Fig. 16. Under deterministic flow, the model having a nonlinear structure under attached flow conditions has zero fatigue damage below $U = 6.3$, as the structure has a fixed point response in that regime. Similarly, under dynamic stall conditions, linear and nonlinear models have zero damage values below U = 5.7. The order of damage is seen to be increasing with flow speed. It is found highest for the model having aerodynamic nonlinearity and linear structure and least for the model with a nonlinear structure under attached flow conditions. It is observed that the damage caused by pure aerodynamic nonlinearity is approximately 30 times more than that caused by pure structural nonlinearity, while coupling the structural nonlinearity into the aerodynamic nonlinearity almost halves the fatigue damage for the structural parameters considered in this study. Thus cubic hardening structural nonlinearity plays a significant role in reducing fatigue damage. **This is attributed to the fact that the structure becomes stiffer with deformation due to the inherent property of structure possessing a hardening type of nonlinearity.** On the other hand, nonlinearities arising from the flow are seen to aggravate the fatigue damage severely. A detailed fatigue-based design is thus essential for aeroelastic systems, such as blades of wind turbines and helicopters, which are highly prone to dynamic stall phenomenon.

4.2.2. Fatigue damage under stochastic conditions

Finally, fatigue damage analysis is done for different nonlinear systems under the effect of fluctuating inflow. Due to the stochastic modeling, actual fatigue damage incurred due to aeroelastic instability is always uncertain. However, statistical data can be collected by changing several stochastic parameters like time scale and fluctuation intensity. Under stochastic inflow, fatigue damage is found to be higher as compared to that under deterministic flow.

For nonlinear structure under attached flow, variation in fatigue damage values under '*Type A*' (Fig. 17(a)) and '*Type B*' (Fig. 17(b)) inflow, are seen to be less affected by intensity variation as compared to those under '*Type C*' inflow (Fig. 17(c)). For $\sigma = 0.1$, the damage values are only slightly higher than fatigue under deterministic flow while for $\sigma = 0.3$, the damage is 100 times higher. Also at $\sigma = 0.3$, significant damage is accumulated even below flutter speed which is a point of concern from the structural health perspective. Under '*Type C*' inflow, maximum fatigue damage obtained at $\sigma = 0.3$ is almost 30 times of that obtained at $\sigma = 0.1$, while for '*Type A*' inflow, its only twice as high at $\sigma = 0.3$ as compared to that at $\sigma = 0.1$.

For the model with pure aerodynamic nonlinearity, the damage variation is shown for '*Type A*', '*Type B*' and '*Type C*' inflow in Fig. 18. Accumulated damage is seen to be almost 60 times higher

Table 3: Maximum value (in MPa) of σ_{zz}, σ_{zx}, σ_{zy}, σ_v and RFC under fluctuating inflow at $\sigma = 0.3$ and $U_m = 7$.

Aeroelastic model	Inflow type	$\sigma_{\mathbf{zz}}$	$\sigma_{\mathbf{zx}}$	$\sigma_{\mathbf{zy}}$	$\sigma_{\mathbf{v}}$	RFC
Attached flow/nonlinear structure	'*Type A*'	9.48	30.39	0.21	53.00	294
	'*Type B*'	12.18	38.69	0.28	70.08	291
	'*Type C*'	12.47	52.19	0.37	91.07	284
Nonlinear aerodynamics/linear structure	'*Type A*'	10.18	42.16	0.28	72.17	373
	'*Type B*'	28.86	49.29	0.38	98.30	349
	'*Type C*'	28.50	88.47	0.64	158.71	303
Coupled structural/aerodynamic nonlinearity	'*Type A*'	13.88	39.02	0.27	66.30	406
	'*Type B*'	13.25	42.85	0.31	76.46	387
	'*Type C*'	21.49	61.19	0.44	107.06	373

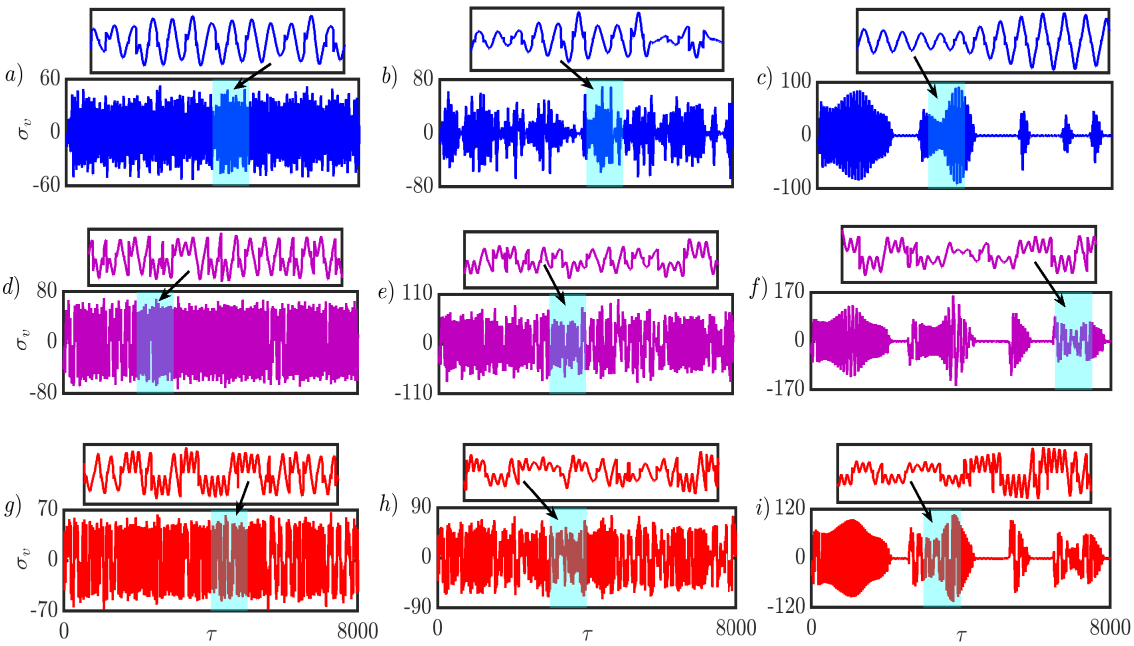

Figure 15: Sample time histories of σ_v (MPa) at $\sigma = 0.3$ and $U_m = 7$; for nonlinear structure and linear aerodynamics under (a) '*Type A*' flow, (b) '*Type B*' flow, and (c) '*Type C*' flow; for linear structure and nonlinear aerodynamics under (d) '*Type A*' flow, (e) '*Type B*' flow, and (f) '*Type C*' flow; and for both nonlinear structure and aerodynamics under (g) '*Type A*' flow, (h) '*Type B*' flow, and (i) '*Type C*' flow.

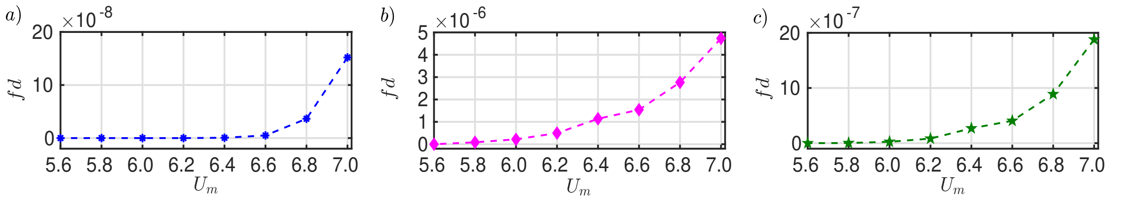

Figure 16: Accumulated damage values under non-fluctuating inflow for (a) Nonlinear structure under attached flow conditions, (b) Linear structure under nonlinear aerodynamic conditions, and (c) Nonlinear structure under nonlinear aerodynamic conditions.

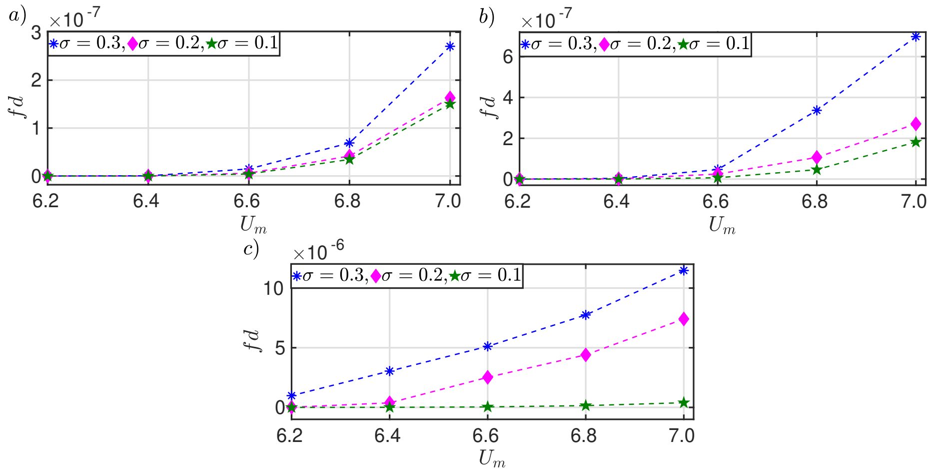

Figure 17: Accumulated damage values under attached flow conditions with the structure possessing cubic hardening nonlinearity in pitch for, (a) '*Type A*' inflow, (b) '*Type B*' inflow, and (c) '*Type C*' inflow.

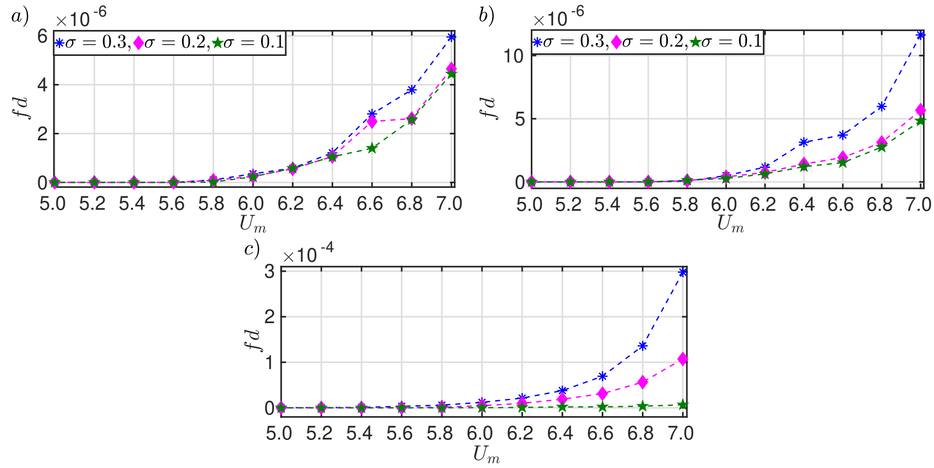

Figure 18: Accumulated damage values under dynamic stall conditions for a linear structure for, (a) '*Type A*' inflow, (b) '*Type B*' inflow, and (c) '*Type C*' inflow.

for '*Type A*' inflow at $U_m = 7$ and $\sigma = 0.3$, as compared to damage values under deterministic flow conditions. While as compared to damage obtained from the model possessing structural nonlinearity under attached flow conditions, the corresponding damage is almost 30 times higher. This indicates the severity of stall flutter problem in the aeroelastic systems, which can be much more dangerous in the presence of material defects like cracks and aging effects. It is quite unrealistic to have an aeroelastic system without any structural nonlinearity. However, the present model with linear structure demonstrates the isolated effect of aerodynamic nonlinearity on its structural health. Next, a more realistic set of fatigue damage results is provided when a coupling between aerodynamic and structural nonlinearity is considered.

Structural stiffness is a major design aspect for aeroelastic systems from both static and dynamic analysis perspectives. For a linear structure, flutter amplitude is diverging, and a hardening nonlinearity in stiffness limits the diverging oscillations to LCOs [3]. In the present study, a similar effect of cubic hardening pitch nonlinearity is observed. When cubic hardening nonlinearity is coupled with aerodynamic nonlinearity, the amplitude of stall flutter LCOs is significantly reduced. Since the present study considers only pitch and plunge deformations to calculate the stresses, the stresses are also reduced significantly by coupling structural nonlinearity to the aerodynamic nonlinearity. However, the number of load levels is also higher in a coupled nonlinear system than in isolated aerodynamic nonlinearity. Hence, a fatigue damage analysis is needed to understand the actual im-

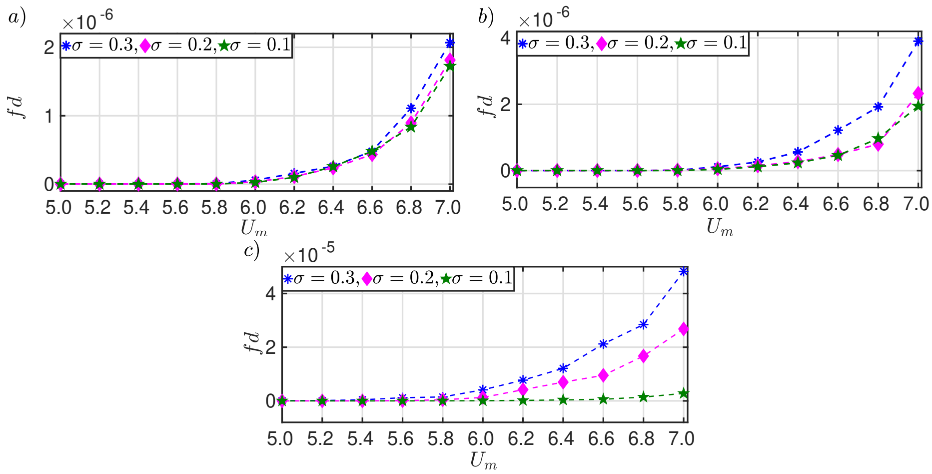

Figure 19: Accumulated damage values under dynamic stall conditions for a nonlinear structure for, (a) '*Type A*' inflow, (b) '*Type B*' inflow, and (c) '*Type C*' inflow.

pact of structural nonlinearity on a system governed by nonlinear aerodynamic loads. Under '*Type A*' inflow (Fig. 19(a)), the damage values are almost similar to those obtained under deterministic conditions and are almost one-third of those obtained for the system under pure aerodynamic nonlinearity. Under '*Type B*' inflow (Fig. 19(b)), the damage values are slightly higher, particularly at $\sigma = 0.3$, the damage values almost double as compared to those under '*Type A*' inflow for same intensity. Damage values are very high under '*Type C*' inflow (Fig. 19(c)) as compared to those under the other two types of inflow, and at $\sigma = 0.3$, the values reach almost 20 times higher as compared to those obtained under deterministic flow for the same nonlinear model. However, the damage values under '*Type C*' inflow for a system with coupled structural and aerodynamic nonlinearity are significantly reduced than that with pure aerodynamic nonlinearity. At $\sigma = 0.3$, the damage incurred by the system under nonlinear aerodynamic load is reduced almost to $1/6^{th}$ with the addition of cubic hardening nonlinearity in structure.

So far, from the numerical simulations, we observe the route to stall flutter in aeroelastic systems depending on the source of nonlinearity and nature of the on-coming wind flows (deterministic/stochastic). For comparison purposes, classical flutter scenarios are as well invoked. From the discerned routes to stall flutter, we compute the fatigue damage incurred under a variety of scenarios. At the interim juncture, we note that the fatigue damage is consistently high for aerodynamic nonlinearities (*i.e.* dynamic stall conditions) irrespective of the deterministic/stochastic nature of the input flow. It is to be reminded to the reader that in hitherto studies, minimal attention has been devoted towards both resolving the intermittency route to stall flutter as well as the structural safety aspect of the same. To glean further into stall-induced fatigue damages in aeroelastic systems, a comparison of our numerical findings with wind tunnel experiments becomes highly necessary.

5. Experimental investigations into stall induced fatigue damage

A preliminary investigation into stall flutter-induced fatigue damage estimated through wind tunnel experiments is presented in this section. The experiments are performed on a NACA 0012 airfoil in a low speed Eiffel type wind tunnel with closed test section (see Fig. 20 (a)). A photograph of the experimental setup inside the wind tunnel test section (dimensions 0.8 m x 0.8 m x 1.2 m) is shown in Fig. 20(b). The airfoil has a span of 0.5 m, chord length of 0.1 m, and is mounted horizontally at the quarter chord in the experimental mechanism. The mechanism is akin to that in Venkatramani *et al.* [53, 27] and its details are not repeated here for brevity sake. A static experiment is performed to obtain load vs deflection curves for plunge (Fig. 20(c)) and pitch (Fig. 20(d)) stiffness, respectively and both the modes show approximately linear stiffness behaviour. A pair of laser displacement sensors having a Wenglor make, and a resolution of one micron, and a displacement range of 50-350 mm is used to obtain the pitch and plunge displacements of the airfoil. A pair of

Table 4: The structural parameters for the experiment. m_y and m_α represent the total moving mass in plunge and pitch respectively and f_y and f_α represents the natural frequency of plunge and pitch mode, respectively (estimated from static experiments).

Parameter	m_y (kg)	m_α (kg)	f_y (Hz)	f_α (Hz)	a_h	I_α (kg-m^2)
Value	1.908	0.937	2.28	4.01	-0.5	0.0017

Delta HD 4V3 TS3 type air velocity sensors are used to the perpetual acquisition of the flow velocity in the wind tunnel test section. Additionally, a stand-alone hot wire anemometer is used to monitor the flow velocities inside the test section. An ATALON data acquisition system is used for acquiring the flow-velocity and the displacement values from the laser sensors as well. The maximum speed achievable in the wind tunnel is approximately 25 m/s. By installing remote controllers over the tunnel fan, the direction of wind flow can be changed from suction to blowing mode.

Under the suction mode of operation, the flows are largely sterile and free from fluctuations (holding true both for empty test section and in the presence of experimental setup - albeit that the latter case understandably gives rise to a larger turbulence intensity). The turbulence intensity under suction mode - obtained from flow data measured using hot-wire anemometers - is less than 1% in the empty section. The blowing mode of tunnel fan operation, on the other hand, gives rise to flows that do not pass via honeycomb meshes, and rather give rise to fluctuating input flows to the test section. Further details about the same can be found in Venkatramani *et al.* [53, 27]. While anemometers help us obtain turbulence intensities at different points, we refrain from explicitly quoting the turbulence intensity in this case as we feel that the full information of flow fluctuations in the test section can be best discerned from particle image velocimetry (PIV) - which is unavailable with us. In wake of turbulence levels, varying point to point in the test section, as well as varying for increasing levels of mean flow speed, we feel it is premature and incomplete to provide turbulence levels in this case. However, given that the focus of the study involves both deterministic (sterile) and stochastic (fluctuating) flows, we show two sample wind time histories below for the sake of readers' clarity. As shown in Fig. 21, the flow data obtained under suction conditions at speed (V) = 14.11 m/s is predominantly invariant with time. On the other hand, the flow time history at mean speed (V_m) = 14.16 m/s measured under blowing conditions shows much higher fluctuations. The turbulence intensity for this case, computed in a simplistic manner as the ratio of the variance of the random process upon the mean value, gives an intensity of 2.65%. Note that the wind profile qualitatively and quantitatively changes at various points inside the test section and also varies considerably with an increase in the mean flow speed. However, quantifying the same is beyond the scope of the present study.

Subsequent to characterizing the static parameters associated with the experimental frameware (see Table 4), we carry out dynamic experiments under suction mode of fan operation. The flow speed (V) is varied systematically from zero to the critical flow speed in which we encounter the onset of LCOs. The initial angle of attack of the airfoil is 6°, which is well below the static stall angle of NACA 0012 [16]. Large amplitude LCOs is observed at $V = 13.82$ m/s; see Figs. 22(a) and 22(b). The LCO amplitudes for the pitch DoF are very high and possibly can be attributed to flow separation and dynamic stall [7, 12, 8]. The frequencies of pitch and plunge oscillations coalesce at the pitch natural frequency (= 4.01 Hz); see Fig. 22(c). This confirms that the oscillations are pitch dominant and can be characterized as stall flutter. It's worth mentioning that the pitch and plunge springs behave linearly (see Fig. 20(c) and Fig. 20(d)) and hence the contribution of structural nonlinearity can be assumed as insignificant.

Figure 23 shows the pitch responses of airfoil under blowing conditions from the velocity range 13.18 - 15.97 m/s. It is observed that airfoil undergoes random oscillations of significant amplitudes at $V = 13.18$ m/s (Fig. 23(a)), which is well below the flutter speed (13.82 m/s). Upon increasing the speed to 14.16 m/s (Fig. 23(b)), the random LCOs grow in amplitude, and at 14.93 m/s, large amplitude random LCOs are observed (Fig. 23(c)). Finally at 15.97 m/s, the amplitude of the

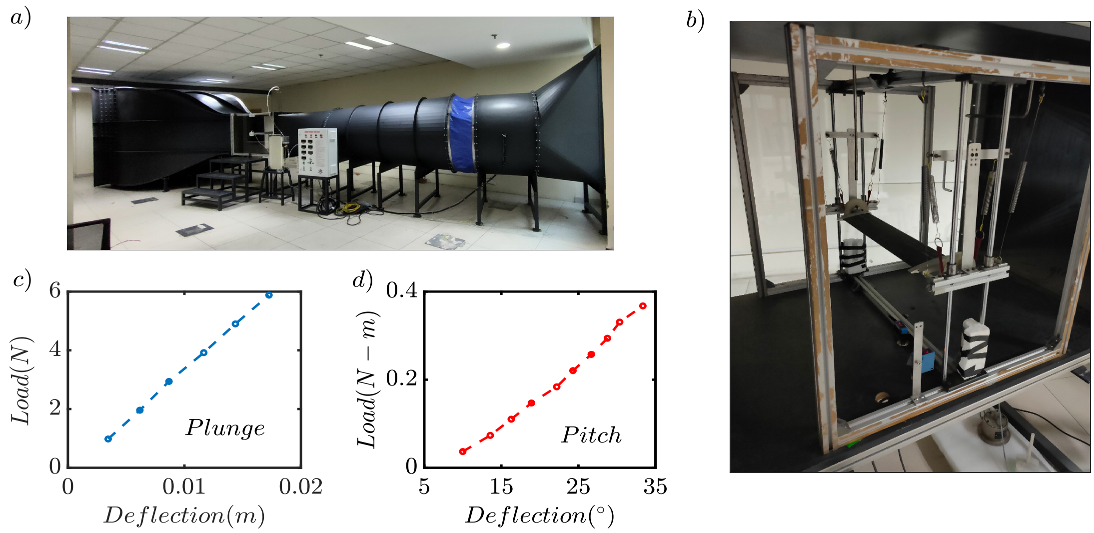

Figure 20: Photographs of the experimental setup; a) Wind tunnel; b) NACA 0012 airfoil in wind tunnel test section along with sensors. Fig. (c) and Fig. (d) represent the load vs deflection plot for plunge and pitch stiffness respectively, which are estimated from the static experiments.

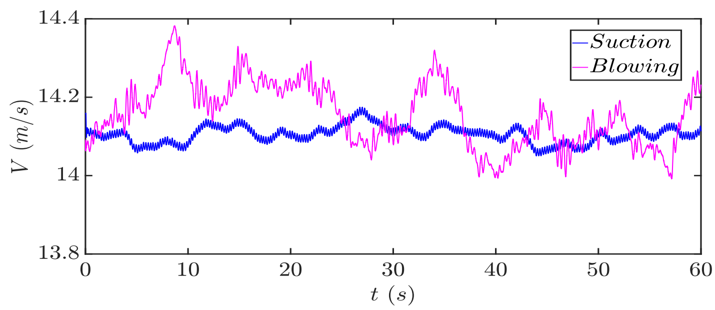

Figure 21: Sample time history of flow variation under suction and blowing conditions.

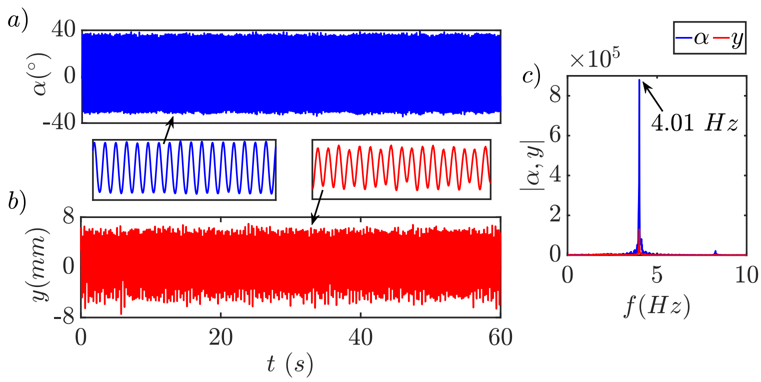

Figure 22: Experimentally obtained responses of NACA 0012 airfoil under suction conditions at stall flutter onset (V = 13.82 m/s) ; a) Pitch response, b) Plunge response, c) Coalescence of pitch and plunge frequencies at pitch natural frequency confirming pitch dominant LCOs.

Table 5: Maximum value of σ_v (in MPa) and accumulated fatigue damage values calculated from experimentally obtained airfoil responses using experimental structural parameters (0.5 m span and 0.1 m chord).

Operating conditions	**flow speed**	σ_v	fd
Suction	13.82	215.94	0.50
Suction	14.63	221.35	0.55
Blowing	13.18	50.11	2.32×10^{-8}
Blowing	14.16	62.43	1.70×10^{-7}
Blowing	14.93	170.94	1.40×10^{-2}
Blowing	15.97	211.24	0.19

random LCOs further increases and becomes more uniform (Fig. 23(d)). Akin to section 4, the stress time histories are obtained from airfoil responses using the same methodology i.e. the airfoil is assumed to be a cantilever structure of 0.1 m chord and 0.5 m span subjected to multiaxial loading. The material properties are same as mentioned in Section 4. Obtained von Mises stresses are presented in Fig. 24. The maximum values of von Mises stresses at various flow speeds are tabulated in Table 5, which are below the material yield strength and their order is similar to those obtained numerically, albeit slightly higher. For the numerical model with pure aerodynamic nonlinearity, the maximum von Mises stress is 158.71 MPa (see Table 3), while for experimentally observed stall induced instability, the maximum von Mises stress is obtained as 221.35 MPa (see Table 5). One of the reasons for higher stresses obtained in experimental framework is perhaps the size of the structure. Since performing wind tunnel experiments in such a big structure, akin to the numerical model, is beyond the capacity under current experimental facilities, we take a miniature blade model and perform similar analysis.

Next, we embark into the estimated fatigue damage obtained from the von Mises stresses. Here we present two cases under suction conditions, and four cases under blowing conditions. The damage is calculated from 60 sec stress data and is presented in Table 5. Although there is significant damage under blowing conditions at $V_m = 13.18$ m/s, which is below the flutter point (13.82 m/s), we see that the fatigue damage caused under suction condition is much higher. Hence for current set of experimental conditions, deterministic inflow (suction) causes more damage as compared to stochastic inflow (blowing). Its worth mentioning that the fatigue damage is highly dependent upon the probabilistic markers namely intensity and time scale of stochastic inflow as shown in subsection 4.2.2. In fact, observing Fig. 16(b) and Fig. 18(a) from numerical analysis, which are cases of pure aerodynamic nonlinearity (akin to experimental case), we see that the fatigue damage values under deterministic conditions (Fig. 16(b)) are higher than those under stochastic conditions (Fig. 18) specifically for low intensity and short time scale conditions, which is possibly the case under blowing experiments also and hence we observe lower fatigue than the suction conditions.

6. Concluding remarks

This study is focused on estimating the effect of nonlinearity originating from various sources under stochastic flow conditions on the aeroelastic responses and associated fatigue damage. Nonlinearity arising from the structure is modeled as cubic hardening pitch stiffness; whereas, the aerodynamic nonlinearity is modeled using LB dynamic stall model. Uncertainties in the oncoming flow are incorporated by modeling the inlet velocity as a stochastic process using KLE with different time scales and intensities. From the same, the following salient findings emerge.

- First, the dynamical signatures of the system under deterministic and stochastic flow conditions are presented by considering isolated cases of nonlinearities and then by studying the combined effects. Under deterministic flow, the bifurcation plots show distinct dynamical behavior under different types of nonlinearity. For a nonlinear structure under attached flow conditions, fixed point response transitions to LCO via a Hopf bifurcation, while for a linear structure under

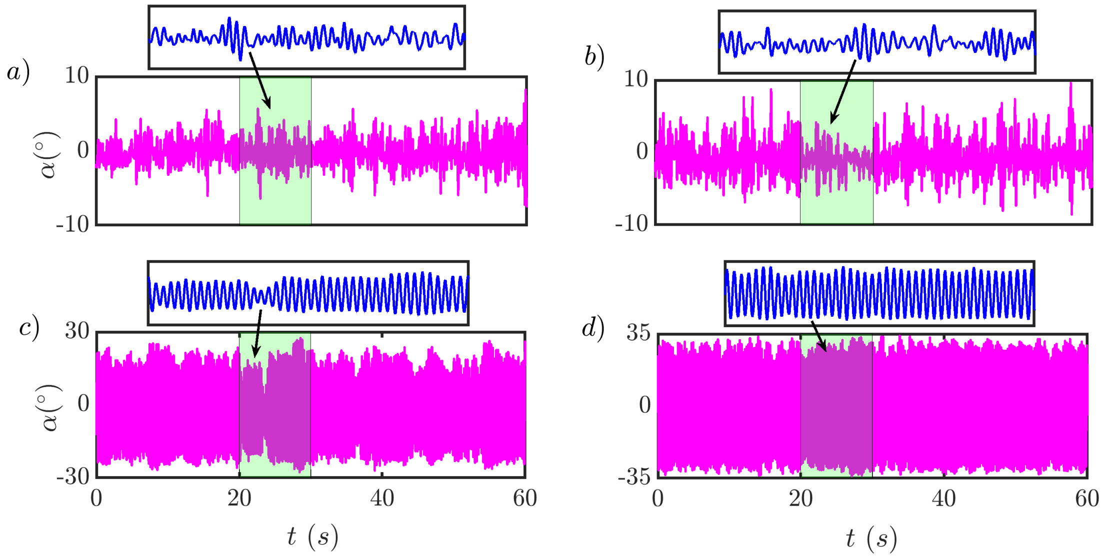

Figure 23: Experimentally obtained pitch responses (in radians) of NACA 0012 airfoil under blowing conditions at; a) V = 13.18 m/s, b) V = 14.16 m/s, c) V = 14.93 m/s, d) V = 15.97 m/s, showing transitions from random LCOs to fully developed LCOs as the flow speed is increased

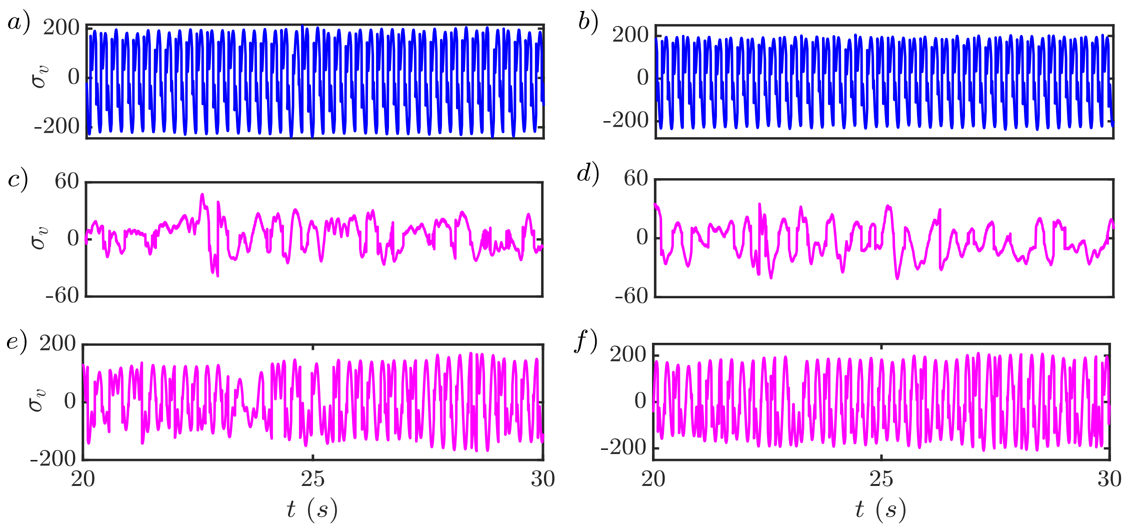

Figure 24: Sample time histories of von Mises stresses calculated from experimentally obtained pitch-plunge responses; under suction conditions a) at V = 13.82 m/s and b) at V = 14.63 m/s; under blowing conditions c) at V = 13.18 m/s, d) at V = 14.16 m/s, e) at V = 14.93 m/s and f) at V = 15.97 m/s.

aerodynamic nonlinearity, stall induced aperiodic oscillations presage LCOs. Under combined effects of structural and aerodynamic nonlinearity, distinct regimes of period-1, period-3, and aperiodic oscillations are observed prior to the onset of stall-induced LCOs.

- Accounting for random fluctuation in the flow gives rise to far more complex signatures, and the qualitative nature of the responses gets largely altered compared to the deterministic cases. The responses under fluctuating flow conditions are governed by the time scale and intensity of fluctuating inflow. Under short time scale input flows, the response signatures depict "burst-type" intermittency. Under long time scale input flows, the responses exhibit an "on-off" intermittency phenomenon. Thus, distinct signatures are present in aeroelastic responses under different nonlinearity and stochastic inflow conditions.

- Using this as an impetus, the system is next investigated from the standpoint of structural safety by estimating the fatigue damage accumulation in the presence of different nonlinearities and inflow conditions. Under stochastic conditions, it is observed that a cubic hardening nonlinear stiffness behavior in the structure can potentially reduce the magnitude of induced stresses. At the same time, the presence of aerodynamic nonlinearity has an adverse effect on stress levels.

- Next, it is demonstrated that the fatigue damage depends on the mean flow speed, fluctuation intensity, and correlation length of stochastic inflow. A comparison between damage-velocity plots for different nonlinear models shows much higher damage values when nonlinearity is purely aerodynamic than cases with purely structural or coupled nonlinearity.

- Finally, we analyze stall-induced instability and subsequent fatigue damage in the deterministic and stochastic frameworks through wind tunnel experiments. Under suction conditions, large-amplitude LCOs are obtained, which are characterized as stall flutter from frequency analysis. On the other hand under blowing conditions, random LCOs are observed below the flutter point which culminates into well-developed LCOs as the flow speed is increased. Specifically, an intermittency route to stall flutter is observed from the experiments as well.

- Fatigue damage analysis from experimental responses shows higher damages owing to stall-induced oscillations - underscoring the larger damages incurred under torsionally dominant oscillations. While the numerics specifically underscored the role of noise intensity and time scale of the flow fluctuations over the fatigue accumulation, the framework of experiments was restrictive for us to depict the same.

  Indeed, the change of noise intensity and scales of input stochastic wind, and in-turn measuring it demand stand alone attention. Nevertheless, both the numerical and experimental findings concur that stall-induced oscillations can impart substantial fatigue damage to the aeroelastic structure.

Given that nonlinearities and random temporal flows are ubiquitous in a suite of aeroelastic problems such as aircraft wings, wind turbine blades, helicopter blades, and even in problems involving bridge-decks, the findings documented in this study carry relevance from the purview of structural safety. Although, the aeroelastic community has heuristically been aware of the impact of stochasticity and nonlinearities in jeopardizing structural safety, minimal efforts to quantify the same are available so far. In that retrospect, this is perhaps the first study to systematically investigate the effect of different nonlinearities and stochastic conditions on fatigue damage of the aeroelastic system *visa a vis* the response dynamics. However, it must be cautioned to the reader that the practicability of the findings presented here to in-field problems involving diverse flow-structural interactions might require further investigations. **Present study considers only cubic hardening nonlinearity in structure. Similar studies considering structural nonlinearities giving raise to subcriticality is indeed an interesting topic and requires a separate study. The complexities arising in fatigue damage estimation due to coexisting attractors due to subcriticality is interesting problem to address. The authors aim for the same in a subsequent study.** This study, as a starting step, is undertaken for a prismatic blade model under uniformly distributed fluid loading with isotropic material properties. Extending the present findings to anisotropic wings (akin to [57]) and even to isotropic structures with material uncertainties (akin to [19]) requires fresh investigations. **The robustness of the analysis can be improved by using CFD solvers to incorporate effects of 3D flow-field behaviour as well as finite element based solvers to capture aeroelastic responses more accurately.** Furthermore, the present study restricts the flow fluctuations to the axial direction. However, it is typical in the aeroelastic community to assign a larger for the random vertical gust [47] over both the response dynamics and the associated impact on structural health. These are very interesting open problems to be taken up by the authors in the future.

Acknowledgments

The authors gratefully acknowledge the funding received from Science and Engineering Research Board (SERB) - start up research grant (SRG-2019- 000077) towards this research.

Declaration of competing interest

The authors declare that they have no known competing financial interests or personal relationships that could have appeared to influence the work reported in this paper.

References

[1] G. Dimitriadis, Introduction to nonlinear aeroelasticity, John Wiley & Sons, 2017.

[2] C. Riso, C. E. Cesnik, B. I. Epureanu, Output-based flutter bifurcation forecasting in nonlinear fluid-structural systems with multiple varying parameters, Journal of Fluids and Structures 101 (2021) 103201.

[3] B. Lee, S. Price, Y. Wong, Nonlinear aeroelastic analysis of airfoils: bifurcation and chaos, Progress in Aerospace Sciences 35 (3) (1999) 205–334.

[4] S. Li, L. Caracoglia, Surrogate model monte carlo simulation for stochastic flutter analysis of wind turbine blades, Journal of Wind Engineering and Industrial Aerodynamics 188 (2019) 43–60.

[5] L. Wang, R. Quant, A. Kolios, Fluid structure interaction modelling of horizontal-axis wind turbine blades based on cfd and fea, Journal of Wind Engineering and Industrial Aerodynamics 158 (2016) 11–25.

[6] L. Wang, X. Liu, A. Kolios, State of the art in the aeroelasticity of wind turbine blades: Aeroelastic modelling, Renewable and Sustainable Energy Reviews 64 (2016) 195–210.

[7] G. Dimitriadis, J. Li, Bifurcation behavior of airfoil undergoing stall flutter oscillations in low-speed wind tunnel, AIAA Journal 47 (11) (2009) 2577–2596.

[8] D. Poirel, L. Goyaniuk, A. Benaissa, Frequency lock-in in pitch–heave stall flutter, Journal of Fluids and Structures 79 (2018) 14–25.

[9] S. Sarkar, H. Bijl, Nonlinear aeroelastic behavior of an oscillating airfoil during stall-induced vibration, Journal of Fluids and Structures 24 (6) (2008) 757–777.

[10] U. Galvanetto, J. Peiro, C. Chantharasenawong, An assessment of some effects of the nonsmoothness of the leishman–beddoes dynamic stall model on the nonlinear dynamics of a typical aerofoil section, Journal of Fluids and Structures 24 (1) (2008) 151–163.

[11] R. M. G. d. Vasconcellos, D. d. A. Pereira, F. D. Marques, Characterization of nonlinear behavior of an airfoil under stall-induced pitching oscillations, Journal of Sound and Vibration 372 (2016) 283–298.

[12] C. R. dos Santos, D. A. Pereira, F. D. Marques, On limit cycle oscillations of typical aeroelastic section with different preset angles of incidence at low airspeeds, Journal of Fluids and Structures 74 (2017) 19–34.

[13] S. Vishal, A. Raaj, C. Bose, J. Venkatramani, Routes to synchronization in a pitch-plunge aeroelastic system with coupled structural and aerodynamic nonlinearities, International Journal of Non-Linear Mechanics (2021) 103766.

[14] R. V. Bethi, S. V. Gali, J. Venkatramani, Response analysis of a pitch–plunge airfoil with structural and aerodynamic nonlinearities subjected to randomly fluctuating flows, Journal of Fluids and Structures 92 (2020) 102820.

[15] H. Devathi, S. Sarkar, Study of a stall induced dynamical system under gust using the probability density evolution technique, Computers & Structures 162 (2016) 38–47.

[16] L. dos Santos, F. Marques, Nonlinear aeroelastic analysis of airfoil section under stall flutter oscillations and gust loads, Journal of Fluids and Structures 102 (2021) 103250.

[17] P. Chaviaropoulos, Flap/lead–lag aeroelastic stability of wind turbine blade sections, Wind Energy: An International Journal for Progress and Applications in Wind Power Conversion Technology 2 (2) (1999) 99–112.

[18] F. Rasmussen, M. H. Hansen, K. Thomsen, T. J. Larsen, F. Bertagnolio, J. Johansen, H. A. Madsen, C. Bak, A. M. Hansen, Present status of aeroelasticity of wind turbines, Wind Energy: An International Journal for Progress and Applications in Wind Power Conversion Technology 6 (3) (2003) 213–228.

[19] S. Venkatesh, S. Sarkar, I. Rychlik, Uncertainties in blade flutter damage prediction under random gust, Probabilistic Engineering Mechanics 36 (2014) 45–55.

[20] Y. L. Xu, T. Liu, W. Zhang, Buffeting-induced fatigue damage assessment of a long suspension bridge, International Journal of Fatigue 31 (3) (2009) 575–586.

[21] G. Georgiou, A. Manan, J. E. Cooper, Modeling composite wing aeroelastic behavior with uncertain damage severity and material properties, Mechanical Systems and Signal Processing 32 (2012) 32–43.

[22] S. Sarkar, S. Gupta, I. Rychlik, Wiener chaos expansions for estimating rain-flow fatigue damage in randomly vibrating structures with uncertain parameters, Probabilistic Engineering Mechanics 26 (2) (2011) 387–398.

[23] J. A. Witteveen, S. Sarkar, H. Bijl, Modeling physical uncertainties in dynamic stall induced fluid–structure interaction of turbine blades using arbitrary polynomial chaos, Computers & Structures 85 (11-14) (2007) 866–878.

[24] B. H. Lee, L. Liu, Bifurcation analysis of airfoil in subsonic flow with coupled cubic restoring forces, Journal of Aircraft 43 (3) (2006) 652–659.

[25] J. Venkatramani, S. K. Kumar, S. Sarkar, S. Gupta, Physical mechanism of intermittency route to aeroelastic flutter, Journal of Fluids and Structures 75 (2017) 9–26.

[26] J. Venkatramani, S. Sarkar, S. Gupta, Intermittency in pitch-plunge aeroelastic systems explained through stochastic bifurcations, Nonlinear Dynamics 92 (3) (2018) 1225–1241.

[27] J. Venkatramani, S. Sarkar, S. Gupta, Investigations on precursor measures for aeroelastic flutter, Journal of Sound and Vibration 419 (2018) 318–336.

[28] C. Bose, S. Gupta, S. Sarkar, Transition to chaos in the flow-induced vibration of a pitching–plunging airfoil at low reynolds numbers: Ruelle–takens–newhouse scenario, International Journal of Non-Linear Mechanics 109 (2019) 189–203.

[29] M. H. Hansen, M. Gaunaa, H. A. Madsen, A beddoes-leishman type dynamic stall model in state-space and indicial formulations, Tech. rep., Risoe National Lab., Roskilde (Denmark) (2004).

[30] J. G. Leishman, T. Beddoes, A semi-empirical model for dynamic stall, Journal of the American Helicopter Society 34 (3) (1989) 3–17.

[31] J. Leishman, K. Nguyen, State-space representation of unsteady airfoil behavior, AIAA Journal 28 (5) (1990) 836–844.

[32] I. Rychlik, A new definition of the rainflow cycle counting method, International Journal of Fatigue 9 (2) (1987) 119–121.

[33] M. A. Miner, Cumulative damage in fatigue, Journal of Applied Mechanics 12 (3) (1945) A159–A164.

[34] A. Palmgren, Die lebensdauer von kugellagern, VDI Zeitschrift 68 (1924) 339–341.

[35] J. Leishman, T. Beddoes, A generalised model for airfoil unsteady aerodynamic behaviour and dynamic stall using the indicial method, in: Proceedings of the 42nd Annual forum of the American Helicopter Society, Washington DC, 1986, pp. 243–265.

[36] R. G. Ghanem, P. D. Spanos, Stochastic finite elements: a spectral approach, Courier Corporation, 2003.

[37] A. Rounak, S. Gupta, Stochastic p-bifurcation in a nonlinear impact oscillator with soft barrier under ornstein–uhlenbeck process, Nonlinear Dynamics 99 (4) (2020) 2657–2674.

[38] K. McAlister, S. Pucci, W. McCroskey, L. Carr, An experimental study of dynamic stall on advanced airfoil sections. volume 2. pressure and force data, Tech. rep., NASA. TM 84245 (1982).

[39] R. P. L. Nijssen, Fatigue life prediction and strength degradation of wind turbine rotor blade composites, Ph.D. thesis, Faculty of Aerospace Engineering, T.U. Delft (2006).

[40] M. Matsuishi, T. Endo, Fatigue of metals subjected to varying stress, in: Proceedings Kyushi Branch JSME, Vol. 68, 1968, pp. 37–40.

[41] N. Dowling, Fatigue failure predictions for complicated stress-strain histories, Journal of Materials 7 (1) (1972) 71–87.

[42] S. D. Downing, D. Socie, Simple rainflow counting algorithms, International Journal of Fatigue 4 (1) (1982) 31–40.

[43] H. French, Fatigue and the hardening of steels, Transactions of the American Society for Steel Treating 21 (1933) 899–946.

[44] B. Langer, Fatigue failure from stress cycles of varying amplitude, Journal of Applied Mechanics 4 (4) (1937) A160–A162.

[45] A. Fatemi, L. Yang, Cumulative fatigue damage and life prediction theories: a survey of the state of the art for homogeneous materials, International Journal of Fatigue 20 (1) (1998) 9–34.

[46] L. Pook, Why Metal Fatigue Matters, Springer, 2007.

[47] D. C. Poirel, Random dynamics of a structurally nonlinear airfoil in turbulent flow, Ph.D. thesis (2001).

[48] S. K. Kumar, S. Sarkar, S. Gupta, Multiplicative noise induced intermittency in maps, International Journal of Non-Linear Mechanics 117 (2019) 103251.

[49] J. Venkatramani, V. Nair, R. Sujith, S. Gupta, S. Sarkar, Multi-fractality in aeroelastic response as a precursor to flutter, Journal of Sound and Vibration 386 (2017) 390–406.

[50] V. Nair, G. Thampi, S. Karuppusamy, S. Gopalan, R. Sujith, Loss of chaos in combustion noise as a precursor of impending combustion instability, International journal of spray and combustion dynamics 5 (4) (2013) 273–290.

[51] V. Nair, R. Sujith, Multifractality in combustion noise: predicting an impending combustion instability, Journal of Fluid Mechanics 747 (2014) 635–655.

[52] V. Nair, G. Thampi, R. Sujith, Intermittency route to thermoacoustic instability in turbulent combustors, Journal of Fluid Mechanics 756 (2014) 470–487.

[53] J. Venkatramani, V. Nair, R. Sujith, S. Gupta, S. Sarkar, Precursors to flutter instability by an intermittency route: a model free approach, Journal of Fluids and Structures 61 (2016) 376–391.

[54] C. Braccesi, F. Cianetti, G. Lori, D. Pioli, An equivalent uniaxial stress process for fatigue life estimation of mechanical components under multiaxial stress conditions, International Journal of Fatigue 30 (8) (2008) 1479–1497.

[55] A. Carpinteri, M. De Freitas, A. Spagnoli, Biaxial/Multiaxial fatigue and fracture, Elsevier, ESIS Publication, 2003.

[56] P. A. Brodtkorb, P. Johannesson, G. Lindgren, I. Rychlik, J. Ryden, E. Sjö, et al., Wafo-a matlab toolbox for analysis of random waves and loads, in: The tenth international offshore and polar engineering conference, International Society of Offshore and Polar Engineers, 2000.

[57] M. Amoozgar, R. Ajaj, J. Cooper, The effect of elastic couplings and material uncertainties on the flutter of composite high aspect ratio wings, Journal of Fluids and Structures 108 (2022) 103439.